

Supersonic friction of a black hole traversing a self-interacting scalar dark matter cloud

Alexis Boudon[✉], Philippe Brax, and Patrick Valageas[✉]

Université Paris-Saclay, CNRS, CEA, Institut de physique théorique, 91191, Gif-sur-Yvette, France

 (Received 16 August 2023; accepted 13 October 2023; published 15 November 2023)

Black holes (BHs) traversing a dark matter cloud made out of a self-interacting scalar soliton are slowed down by two complementary effects. At low subsonic speeds, the BH accretes dark matter, and this is the only source of dragging along its motion, if we neglect the backreaction of the cloud's self-gravity. The situation changes at larger supersonic speeds where a shock appears. This leads to the emergence of an additional friction term, associated with the gravitational and scalar pressure interactions and with the wake behind the moving BH. This is a long distance effect that can be captured by the hydrodynamical regime of the scalar flow far away from the BH. This dynamical friction term has the same form as the celebrated Chandrasekhar collisionless result, albeit with a well-defined Coulomb logarithm and a prefactor that is smaller by a factor $2/3$. The infrared cutoff is naturally provided by the size of the scalar cloud, which is set by the scalar mass and coupling, whilst the ultraviolet behavior corresponds to the distance from the BH where the velocity field is significantly perturbed by the BH, which is determined by pressure effects. As a result, supersonic BHs are slowed down by both the accretion drag and the dynamical friction. This effect will be potentially detectable by future gravitational wave experiments as it influences the phase of the gravitational wave signal from inspiralling binaries.

DOI: [10.1103/PhysRevD.108.103517](https://doi.org/10.1103/PhysRevD.108.103517)

I. INTRODUCTION

The Λ CDM model is the present established cosmological framework providing a comprehensive description of the Universe's large-scale structure and evolution. Central to this model is cold dark matter (CDM), a nonrelativistic component that exerts a significant gravitational influence, shaping the formation of galaxies and galaxy clusters. CDM constitutes approximately 27% of the total energy content of the Universe [1,2] and plays a crucial role in the clumping and development of cosmic structures under gravitational effects.

Despite its success in explaining various cosmological observations, the standard CDM paradigm encounters challenges at smaller scales. Direct detection experiments focusing on weakly interacting massive particles [3–8], a prominent CDM candidate, are reaching their limitations [9–12]. Moreover, at galactic scales, tensions arise as CDM predictions deviate from observations, manifesting themselves in the core-cusp problem [13–17], the missing satellite problem [18–21], and the too-big-to-fail problem [22–25]. While introducing realistic baryons and baryonic feedback in CDM simulations offers potential solutions, these effects may not be sufficient to explain fully the observed discrepancies. As a result, researchers have explored alternative approaches, including investigating alternative dark matter scenarios such as primordial black holes [26–30], axions [31–36], and sterile neutrinos [37–42], or considering modifications to gravity theories.

The ultralight dark matter paradigm [43–47], particularly fuzzy dark matter (FDM), has emerged as a promising alternative. FDM introduces ultralight scalar particles with masses around 10^{-22} eV, characterized by large de Broglie wavelengths. These particles form solitonic solutions at the centers of dark matter halos [48–75], providing a potential resolution to many of the tensions observed at galactic scales [43–47] while recovering the success of the CDM at cosmological scales [43,76–82]. However, recent observations, including the Lyman- α forest and galaxy rotational curves [65,83–86], constrain the FDM particle mass to be above 10^{-21} eV, suggesting that FDM alone may no longer suffice to resolve fully the smaller-scale cosmological discrepancies.

A closely related alternative is self-interacting scalar-field dark matter (SFDM), where scalar dark matter possesses repulsive self-interactions [48,87–96]. This model offers means to reconcile the success of FDM while introducing distinct behaviors at galactic scales. Within this scenario, solitonic solutions no longer remain in equilibrium solely due to the balance between self-gravity and quantum pressure. Instead, repulsive self-interactions introduce an effective pressure, influencing the equilibrium state. In the Thomas-Fermi regime [97,98], the repulsive self-interactions dominate over quantum pressure, resulting in equilibrium being determined solely by self-gravity and the effective pressure [52]. A promising method to detect possible signs of such dark matter involves studying its

gravitational effects on black hole observations, for example by using gravitational waves [99–101] or observational estimates around black holes (BHs) [102–104].

Dynamical friction and mass accretion play significant roles in astrophysics, impacting various astrophysical phenomena. Extensive research on dynamical friction and mass accretion has been conducted for both FDM [44,105–113] and CDM, treated as collisionless particles [114]. In this context, these investigations have provided valuable insights and constraints on dark matter models, including applications to the Fornax globular cluster timing problem [115], a discrepancy observed in the Fornax galaxy where the expected strong dynamical friction, predicted by the standard CDM model, fails to reproduce the observations of slowly migrating globular clusters toward the galaxy center, and their relevance to gravitational waves where dynamical friction can slow down binary systems and induce phase shifts in gravitational wave emission.

In this paper, we explore the effects of dynamical friction and mass accretion experienced by a Schwarzschild black hole moving within a self-interacting scalar dark matter cloud at supersonic velocities. Our primary focus is on the Thomas-Fermi regime, where self-interactions are significant and the wavelike effects of the scalar field are negligible. This regime results in dark matter dynamics within the solitonic solution behaving more like a gas than FDM, although it retains distinctive characteristics. This study of the supersonic regime complements our previous investigation in the subsonic case [116], offering relevance to ongoing research on gravitational waves. The implications of mass accretion and dynamical friction on binary systems can be critical, potentially detectable by upcoming gravitational wave detectors such as DECIGO or LISA [101,117–120]. Additionally, the application of such results to the Fornax globular cluster timing problem, where the CDM dynamical friction appears too strong, is of particular interest.

The outline of the paper is as follows. Section II introduces scalar-field dark matter with quartic self-interactions, discussing its equations of motion and equilibrium solitonic solutions. Section III compares the subsonic and supersonic regimes and calculates the large-distance expansions of the dark matter flow for both the upstream and downstream regions, including the appearance and location of shock fronts and boundary layers. Section IV describes the relation between these asymptotic expansions and the BH accretion rate and derives the drag force exerted on the BH. Section V discusses the accretion rate in comparison with the radial case and with the classical Hoyle-Lyttleton prediction, and highlights the two regimes obtained at moderate and high Mach numbers. Section VI compares the magnitudes of the accretion drag and dynamical friction, while Sec. VII provides an independent computation of the dynamical friction from the

gravitational force exerted by the BH wake. Section VIII presents a numerical computation of the density and velocity fields for a moderate Mach number, to illustrate the behavior of the system with a bow shock upstream of the BH. Section IX compares our results with the behaviors of other systems (collisionless, perfect fluid and FDM cases). Finally, we conclude our study in Section X.

II. DARK MATTER SCALAR FIELD

A. Scalar-field action

As in our previous work [116], we consider a scalar-field dark matter scenario described by the action

$$S_\phi = \int d^4x \sqrt{-g} \left[-\frac{1}{2} g^{\mu\nu} \partial_\mu \phi \partial_\nu \phi - V(\phi) \right], \quad (1)$$

with a quartic self-interaction,

$$V(\phi) = \frac{m^2}{2} \phi^2 + V_1(\phi) \quad \text{with} \quad V_1(\phi) = \frac{\lambda_4}{4} \phi^4. \quad (2)$$

Here m is the mass of the scalar field and λ_4 its coupling constant, which is taken positive. This corresponds to a repulsive self-interaction, which gives rise to an effective pressure that can balance gravity. This allows the formation of stable static equilibria, also called boson stars or solitons. Thus, in this paper we consider the supersonic motion of a BH inside such an extended soliton, or quasistatic dark matter halo.

The parameters m and λ_4 determine the characteristic density and radius,

$$\rho_a = \frac{4m^4}{3\lambda_4}, \quad r_a = \frac{1}{\sqrt{4\pi\mathcal{G}\rho_a}}. \quad (3)$$

The dynamics that we study in this paper will only depend on this combination ρ_a and on the mass and velocity of the BH. Thus, different dark matter models with the same ρ_a show the same large-scale dynamics. We refer to [116] for a presentation of the regions in the parameter space (m, λ_4) where our computations apply, for various BH masses. We briefly recall below the equations of motion of the scalar field in the relativistic and nonrelativistic regimes.

B. Relativistic regime

As in [116], we neglect the gravitational backreaction of the scalar cloud, and we consider the steady-state limit, that is, the growth and the displacement of the BH are small as compared with the BH mass and the dark matter halo radius. Then, working with the isotropic radial coordinate r , the static spherically symmetric metric can be written as

$$ds^2 = -f(r)dt^2 + h(r)(dr^2 + r^2d\bar{\Omega}^2). \quad (4)$$

Close to the BH, below a transition radius r_{sg} , the BH gravity dominates, and the isotropic metric functions $f(r)$ and $h(r)$ read as

$$\begin{aligned} \frac{r_s}{4} < r \ll r_{\text{sg}}: f(r) &= \left(\frac{1 - r_s/(4r)}{1 + r_s/(4r)} \right)^2, \\ h(r) &= (1 + r_s/(4r))^4, \end{aligned} \quad (5)$$

where $r_s = 2\mathcal{G}M_{\text{BH}}$ is the Schwarzschild radius. In these coordinates, the BH horizon is located at radius $r = r_s/4$. Far from the BH, beyond the transition radius r_{sg} , the dark matter self-gravity dominates but is nonrelativistic, and we have

$$r \gg r_{\text{sg}}: f = 1 + 2\Phi_{\text{N}}, \quad h = 1 - 2\Phi_{\text{N}}, \quad (6)$$

where the Newtonian gravitational potential Φ_{N} is given by the Poisson equation, $\nabla^2\Phi_{\text{N}} = 4\pi\mathcal{G}\rho$.

In the relativistic regime, the scalar-field dynamics are governed by the nonlinear Klein-Gordon equation

$$\frac{\partial^2\phi}{\partial t^2} - \sqrt{\frac{f}{h^3}}\nabla \cdot (\sqrt{fh}\nabla\phi) + f\frac{\partial V}{\partial\phi} = 0. \quad (7)$$

For the spherically symmetric and static metric (4) and the quartic self-interaction (2), one obtains in the large-scalar mass limit the solution [95]

$$\phi = \phi_0(r, \theta)\text{cn}[\omega(r, \theta)t - \mathbf{K}(r, \theta)\beta(r, \theta), k(r, \theta)], \quad (8)$$

where $\text{cn}(u, k)$ is the Jacobi elliptic function [121,122] of argument u , modulus k , and period $4\mathbf{K}$, and $\mathbf{K}(k)$ is the complete elliptic integral of the first kind, defined by $\mathbf{K}(k) = \int_0^{\pi/2} d\theta/\sqrt{1 - k^2 \sin^2\theta}$ for $0 \leq k < 1$ [121,122]. Here we noted $\mathbf{K}(r, \theta) \equiv \mathbf{K}[k(r, \theta)]$. Equation (8) is the leading-order approximation in the limit

$$mr_s \gg 1, \quad (9)$$

that is, the Compton wavelength of the scalar field is much smaller than the BH horizon. We focus on this regime in this paper. The expression (8) means that the usual trigonometric functions encountered in the free case, for a quadratic potential $V(\phi)$, are replaced by the Jacobi elliptic functions in the anharmonic case, when the quartic self-interaction (2) is important. This corresponds to the Duffing equation [123] associated with a cubic nonlinearity. This regime corresponds to a dark matter density $\rho \sim \rho_a$ and a modulus $k \sim 1$. At low density, $\rho \ll \rho_a$, the self-interaction potential is small, we have $k \ll 1$ and the Jacobi elliptic function converges to a trigonometric function as $\text{cn}(u, 0) = \cos(u)$.

Substituting the expression (8) into the Klein-Gordon equation (7) gives the two conditions

$$(\nabla\beta)^2 = \frac{h}{f} \left(\frac{2\omega_0}{\pi} \right)^2 - \frac{hm^2}{(1 - 2k^2)\mathbf{K}^2}, \quad (10)$$

$$\frac{\lambda_4\phi_0^2}{m^2} = \frac{2k^2}{1 - 2k^2}. \quad (11)$$

C. Nonrelativistic regime

In the nonrelativistic weak-gravity regime, it is convenient to write the real scalar field ϕ in terms of a complex field ψ as [44,94]

$$\phi = \frac{1}{\sqrt{2m}} (e^{-imt}\psi + e^{imt}\psi^*). \quad (12)$$

In this regime, where typical frequencies $\dot{\psi}/\psi$ and momenta $\nabla\psi/\psi$ are much smaller than m , the complex scalar field ψ obeys the Schrödinger equation,

$$i\dot{\psi} = -\frac{\nabla^2\psi}{2m} + m(\Phi_{\text{N}} + \Phi_{\text{I}})\psi, \quad (13)$$

where Φ_{I} is the nonrelativistic self-interaction potential, given by

$$\Phi_{\text{I}} = \frac{m|\psi|^2}{\rho_a}. \quad (14)$$

It is also convenient to express ψ in terms of the amplitude ρ and the phase s by the Madelung transformation [52,124],

$$\psi = \sqrt{\frac{\rho}{m}} e^{is}. \quad (15)$$

Then, the real and imaginary parts of the Schrödinger equation (13) give

$$\dot{\rho} + \nabla \cdot \left(\rho \frac{\nabla s}{m} \right) = 0, \quad (16)$$

$$\frac{\dot{s}}{m} + \frac{(\nabla s)^2}{2m^2} = -(\Phi_{\text{N}} + \Phi_{\text{I}}), \quad (17)$$

while the nonrelativistic self-interaction potential reads as

$$\Phi_{\text{I}} = \frac{\rho}{\rho_a}. \quad (18)$$

Defining the curl-free velocity field \vec{v} by

$$\vec{v} = \frac{\nabla s}{m}, \quad (19)$$

Eqs. (16) and (17) give the usual continuity and Euler equations,

$$\dot{\rho} + \nabla \cdot (\rho \vec{v}) = 0, \quad (20)$$

$$\dot{\vec{v}} + (\vec{v} \cdot \nabla) \vec{v} = -\nabla(\Phi_N + \Phi_I). \quad (21)$$

Thus, in the nonrelativistic regime, we can go from the Klein-Gordon equation to the Schrödinger equation and next to an hydrodynamical picture. In this regime, Eq. (10) corresponds to the Bernoulli equation associated with the integrated form of the Euler equation (21), where the velocity reads as

$$\vec{v} = \frac{\pi \nabla \beta}{2m}. \quad (22)$$

In the Hamilton-Jacobi and Euler equations (17) and (21) we neglected the quantum pressure term

$$\Phi_Q = -\frac{\nabla^2 \sqrt{\rho}}{2m^2 \sqrt{\rho}}. \quad (23)$$

This is because we consider masses much greater than 10^{-22} eV, associated with fuzzy dark matter scenarios, so that the de Broglie wavelength $\lambda_{\text{dB}} = 2\pi/mv$ is much smaller than the scales of interest. This implies that wave effects, such as interference patterns, are negligible. However, the dynamics remain different from that of CDM particles because of the self-interaction, which is relevant up to galactic scales and balances gravity, allowing for the formation of stable equilibrium configurations often called solitons. See Ref. [116] for a derivation of the regions in the parameter space $(m, \lambda_4, M_{\text{BH}})$ where our approximations are valid.

D. Nonrelativistic dark matter halo

On large scales, where the BH gravity is negligible as compared with the dark matter self-gravity, the Euler equation (21) admits hydrostatic equilibria, given by $\nabla(\Phi_N + \Phi_I) = 0$. This can be integrated as

$$\Phi_N + \Phi_I = \alpha, \quad \text{with} \quad \alpha = \Phi_N(R_{\text{sol}}). \quad (24)$$

Here we introduced the radius R_{sol} of the spherically symmetric halo, also called soliton, where the density vanishes. In the Thomas-Fermi limit (24) where the quantum pressure (23) is negligible, the solution reads as [52,94,95]

$$r \gg r_{\text{sg}}: \rho(r) = \rho_0 \frac{\sin(r/r_a)}{(r/r_a)} \quad \text{and} \quad R_{\text{sol}} = \pi r_a, \quad (25)$$

and the transition radius r_{sg} is given by

$$r_{\text{sg}} = r_s \frac{\rho_a}{\rho_0} \gg r_s. \quad (26)$$

The bulk density ρ_0 is set by the mass of this dark matter halo, $M_{\text{sol}} = (4/\pi)\rho_0 R_{\text{sol}}^3$. This is the second dark matter parameter, in addition to ρ_a , that enters the dynamics that we study in this paper. It depends on the formation history of the dark matter halo. In this regime, the effective pressure associated with the self-interaction Φ also defines a sound speed c_s given by

$$c_s^2(\rho) = \frac{\rho}{\rho_a} \ll 1, \quad (27)$$

which corresponds to a polytropic gas of adiabatic index $\gamma = 2$. From Eq. (26) we can see that the sound speed in the bulk is also related to the transition radius as

$$r_{\text{sg}} = \frac{r_s}{c_{s0}^2}, \quad c_{s0}^2 = \frac{\rho_0}{\rho_a}. \quad (28)$$

E. Radial accretion

Close to the horizon, the dark matter cannot remain static and falls into the BH. The case of radial accretion around a motionless BH was studied in [95]. Equations (10) and (11) give the phase β and the amplitude ϕ_0 as a function of the modulus $k(r)$. The latter is next obtained from the continuity equation averaged over the scalar oscillations, that is, from the condition of constant flux over all radii in the steady state. Then, as for the Bondi problem of the radial accretion of a perfect gas on a BH, the dark matter profile is determined by the unique transsonic solution that matches the quasistatic equilibrium soliton at large radius and the free fall at the BH horizon. This gives the accretion rate [95]

$$\dot{M}_{\text{BH,radial}} = 3\pi F_\star \rho_a r_s^2 = 3\pi F_\star \rho_0 r_s^2 / c_{s0}^2, \quad (29)$$

where $F_\star \simeq 0.66$. The result (29) means that the dark matter density near the horizon is of the order of the characteristic density ρ_a while the radial velocity is of the order of the speed of light.

This result is much lower than the Bondi accretion $\dot{M}_{\text{Bondi}} \sim \rho_0 r_s^2 / c_{s0}^3$ [125]. This is because the stiff polytropic index $\gamma = 2$ makes the repulsive self-interaction strong enough to slow down the infall significantly. Moreover, in contrast with the Bondi case with $1 < \gamma < 5/3$, the sonic radius r_c where the Mach number $|v_r|/c_s$ reaches unity is located within the relativistic regime, where the hydrodynamical picture is no longer valid and one needs to use the Klein-Gordon equation of motion (7), or its large-mass limit (10) and (11).

F. Isentropic potential flow

Introducing as in [116] the dimensionless variables

$$\hat{r} = \frac{r}{r_s}, \quad \hat{\rho} = 2 \frac{\rho}{\rho_a}, \quad \hat{\beta} = \frac{\pi}{2mr_s} \beta, \quad \vec{v} = \hat{\nabla} \hat{\beta}, \quad (30)$$

the continuity equation (20) and the Bernoulli equation associated with the Euler equation (21) coincide with those of an isentropic potential flow with a polytropic index $\gamma = 2$,

$$\widehat{\nabla} \cdot (\hat{\rho} \vec{v}) = 0, \quad \frac{v^2}{2} + V + H = 0, \quad (31)$$

where the external potential $V(\hat{r})$ and the enthalpy $H(\hat{\rho})$ are given by

$$V(\hat{r}) = -\frac{\hat{\rho}_0}{2} - \frac{v_0^2}{2} - \frac{1}{2\hat{r}}, \quad H(\hat{r}) = \frac{\hat{\rho}}{2}. \quad (32)$$

Here and throughout this paper we work in the BH frame, where the BH is at rest and the dark matter cloud moves at the uniform velocity \vec{v}_0 far from the BH. From the Bernoulli equation (31) the density can be expressed in terms of the velocity by

$$\hat{\rho} = \hat{\rho}_0 + \frac{1}{\hat{r}} + v_0^2 - v^2, \quad (33)$$

and substituting into the continuity equation (31) gives

$$\widehat{\nabla} \cdot \left[\left(\hat{\rho}_0 + \frac{1}{\hat{r}} + v_0^2 - (\widehat{\nabla} \hat{\rho})^2 \right) \widehat{\nabla} \hat{\rho} \right] = 0. \quad (34)$$

This equation holds in the nonrelativistic regime, beyond a radius $r_m \sim 40r_s$.

III. LARGE-DISTANCE EXPANSIONS

A. Subsonic and supersonic regimes

Although it is not possible to obtain the general solution of the nonlinear equation of motion (34), we can derive perturbative expansions in the large-distance limit. This allows us to understand the main properties of the flow and also to obtain analytical results for the BH dynamical friction. Indeed, by conservation of mass and momentum in the steady state, the accretion rate and the drag force are related to the influx of matter and momentum through any surface enclosing the BH, which can be taken to be a sphere of large radius.

1. Subsonic regime

In the subsonic regime, studied in [116], we obtained at large distance an expansion of the form

$$\hat{\rho} = \hat{\rho}_{-1} + \hat{\rho}_0 + \hat{\rho}_1 + \dots, \quad \text{with} \quad \hat{\rho}_n \sim \hat{r}^{-n}, \quad (35)$$

where the dots stand for higher-order terms over $1/\hat{r}$ and

$$\hat{\rho}_{-1} = v_0 \hat{r} u \quad (36)$$

is the leading-order term associated with the uniform flow \vec{v}_0 . In the subsonic case, we then have

$$\text{subsonic} \quad \hat{\beta}_0 = f_0(u), \quad \hat{\beta}_1 = \frac{f_1(u)}{\hat{r}}, \quad (37)$$

where we introduced the angular variable u , defined as

$$u = \cos \theta, \quad (38)$$

and the functions f_n are smooth over $-1 < u < 1$. The first-order correction f_0 is generated by the $1/\hat{r}$ term in Eq. (34), associated with the BH gravity, coupled to the zeroth-order uniform flow $v_0 \hat{u}$. The latter being odd, this gives an odd correction in u . The second-order correction f_1 contains both odd and even terms. In particular, the even term is directly related to the mass and momentum influx at large distance, and thus to the BH mass accretion and dynamical friction. The first-order correction f_0 is obtained by expanding Eq. (34) over $1/\hat{r}$ and collecting the leading-order terms of order $1/\hat{r}^2$. This gives the linear differential equation

$$\frac{\partial^2 \hat{\beta}_0}{\partial \hat{x}^2} + \frac{\partial^2 \hat{\beta}_0}{\partial \hat{y}^2} + \left(1 - \frac{v_0^2}{c_{s0}^2} \right) \frac{\partial^2 \hat{\beta}_0}{\partial z^2} = \frac{v_0 u}{\hat{\rho}_0 \hat{r}^2}, \quad (39)$$

where we work in the Cartesian coordinates, $\{\hat{x}, \hat{y}, \hat{z}\}$, with $\vec{v}_0 = v_0 \vec{e}_z$. As pointed out in [116], in the subsonic regime, $v_0 < c_{s0}$, Eq. (39) is elliptic, whereas in the supersonic regime that we study in this paper, $v_0 > c_{s0}$, Eq. (39) is hyperbolic. In the subsonic regime, this gives a flow that is regular over all space and determined by the boundary conditions at infinity (the uniform velocity \vec{v}_0) and at the center (the matching radius r_m somewhat above the Schwarzschild radius).

2. Supersonic regime

As for hydrodynamical flows around moving bodies, such as airplanes, in the subsonic regime acoustic waves travel faster than the body and are able to propagate to all points in space (after waiting for a long/infinite time as in the steady state). This means that the fluid at any point adapts to the presence of the moving body, the flow is smooth, and it determined by the boundary conditions at infinity and at the surface of the body (in our case the Schwarzschild radius).

At supersonic velocities, acoustic waves cannot catch up with the airplane speed and are deported downstream, within the Mach cone. Then, the flow upstream remains unperturbed and the matching to the boundary conditions on the surface of the airplane is made possible thanks to a shock, which originates at the front tip of the plane or somewhat before. The shock discontinuity provides the means for the flow to jump to a new pattern downstream, which can match the boundary conditions on the plane.

A similar behavior appears in our case, when the BH moves at supersonic speed inside the dark matter cloud. An additional complication is that it is not possible to apply

simple perturbative treatments as in Eq. (35) on both sides of the shock, with junction conditions on the shock. Indeed, we shall see that boundary layers, governed by nonlinear effects, appear on both sides of the shock. Therefore, in the supersonic regime, we must split the large-distance expansions over four domains: (1) the upstream region far before the shock, (2) the boundary layer just before the shock, (3) the boundary layer just after the shock, and (4) the downstream region far behind the shock.

The far upstream and downstream regimes can again be analyzed through large-distance expansions such as (35). As in the subsonic regime, this gives a standard perturbative approach, where each order $\hat{\beta}_n$ obeys a linear differential equation with a right-hand side that involves the lower-order terms $\hat{\beta}_m$ with $m < n$. However, the functions $\hat{\beta}_n$ now take different forms in the upstream and downstream regions, and they may contain logarithmic contributions in $\ln(\hat{r})$. The boundary layers require new expansions, which take into account nonlinearities. The full solution is obtained by matching together these four regions. This involves two asymptotic matchings, between each boundary layer and either the upstream or the downstream bulk flow, and one junction condition along the shock between the two boundary layers. We must also match with the uniform velocity \vec{v}_0 at infinity and simultaneously determine the location of the shock. The matching to the radial inflow at the Schwarzschild radius appears in a natural fashion as a constant of integration. We detail this procedure in the next sections.

B. Upstream region

1. Large-distance expansion

We first consider the far upstream region. As explained above, because of the hyperbolic nature of the equation of motion (39), this is no longer a boundary-value problem (as in the subsonic case) but a Cauchy problem, with an initial condition upstream at $\hat{z} \rightarrow -\infty$. Indeed, Eq. (39) now takes the form of a wave equation,

$$\frac{\partial^2 \hat{\beta}_0}{\partial \hat{x}^2} + \frac{\partial^2 \hat{\beta}_0}{\partial \hat{y}^2} - \frac{1}{c_z^2} \frac{\partial^2 \hat{\beta}_0}{\partial \hat{z}^2} = \frac{v_0 u}{\hat{\rho}_0^2 \hat{r}^2}, \quad (40)$$

with

$$v_0 > c_{s0}: \quad \frac{1}{c_z^2} = \frac{v_0^2}{c_{s0}^2} - 1, \quad c_z > 0, \quad (41)$$

where \hat{z} plays the role of time and c_z the role of the propagation speed.

Far from the boundary layer, the flow is smooth, and we can again write a large-distance expansion as in (35). However, we shall see that the terms $\hat{\beta}_n$ can include logarithmic factors $\ln(\hat{r})$.

2. First-order correction

At large velocities v_0 , the effective pressure in the soliton associated with the term $\hat{\rho}_0$ becomes negligible, and we thus expect to recover the collisionless case. We describe the behavior of fuzzy dark matter [44], that is, scalar-field dark matter without self-interactions, in Appendix A. We first recall in Appendix A 1 the results obtained in the Schrödinger picture, from the classic scattering by a Newton or Coulomb potential [44,126]. Then, we show in Appendix A 2 how this behavior can be recovered from the hydrodynamical approach that we use in this paper. From the expression (A13) obtained in the free case, we can expect a logarithmic dependence on the distance \hat{r} in addition to the angular dependence, due to the long-range character of the Newtonian $1/r$ potential. Then, at first order we look for a solution of the form

$$\hat{\beta}_0 = a \ln(\hat{r}) + f_0(u), \quad (42)$$

where a is a parameter to be determined. Substituting into Eq. (34) and collecting the terms of order $1/\hat{r}^2$, which corresponds to substituting into Eq. (40), we obtain the differential equation

$$(1 - u^2)[(1 + c_z^2)u^2 - 1]f_0'' + u[3 + c_z^2 - 3(1 + c_z^2)u^2]f_0' = \frac{1 + c_z^2}{2v_0}u + a[1 - 2(1 + c_z^2)u^2]. \quad (43)$$

This is a first-order equation in f_0' , with the general solution

$$f_0' = \frac{1 - 2v_0 a u}{2v_0(1 - u^2)} + \frac{b}{(1 - u^2)\sqrt{(1 + c_z^2)u^2 - 1}}, \quad (44)$$

where b is an integration constant. Defining the Mach angle θ_c by

$$0 < \theta_c < \frac{\pi}{2}: \quad \sin \theta_c = \frac{c_z}{\sqrt{1 + c_z^2}} = \frac{c_{s0}}{v_0} = \frac{1}{\mathcal{M}_0}, \quad (45)$$

where \mathcal{M}_0 is the Mach number, which also gives

$$u_c = \cos \theta_c = \frac{1}{\sqrt{1 + c_z^2}}, \quad \tan \theta_c = c_z, \quad (46)$$

the second term in Eq. (44) is singular on the upstream and downstream Mach cones $\theta = \pi - \theta_c$ and $\theta = \theta_c$. To avoid the unphysical upstream singularity at $\pi - \theta_c$, the constant b must be zero. The angular velocity at order $1/\hat{r}$ is $v_{\theta 1} = (-\sin \theta/\hat{r})f_0'(u)$. To avoid a singularity at $\theta = \pi$, along the \hat{z} axis upstream, we must have $a = -1/(2v_0)$. This nonzero value shows that the logarithmic term $a \ln(\hat{r})$ cannot be ignored, and we obtain

$$f'_0(u) = \frac{1}{2v_0(1-u)}, \quad f_0(u) = -\frac{\ln(1-u)}{2v_0}. \quad (47)$$

Here we discarded the irrelevant integration constant in f_0 because the velocity potential $\hat{\beta}$ is defined up to a constant that plays no role, as only gradients $\widehat{\nabla}\hat{\beta}$ appear in the equations of motion. This gives the upstream solution

$$\hat{\beta}_0 = -\frac{\ln(\hat{r} - \hat{z})}{2v_0} = -\frac{\ln[\hat{r}(1-u)]}{2v_0} \quad (48)$$

and

$$v_{r1} = -\frac{1}{2v_0\hat{r}}, \quad v_{\theta1} = -\frac{1+u}{2v_0\hat{r}\sqrt{1-u^2}},$$

$$v_1^2 = \frac{1}{\hat{r}}, \quad \hat{\rho}_1 = 0. \quad (49)$$

Thus, at this first order, we actually recover the long-distance solution of the collisionless case (A12). This is because at this order $1/\hat{r}$, the density is not modified by the deflection of the particle trajectories by the BH, $\hat{\rho}_1 = 0$ (but there will be corrections at higher orders). This implies that at this order there are no pressure effects, because there are no density gradients, and therefore we recover the results obtained for the supersonic motion in plasmas [127] and isothermal gas [128,129].

In contrast with the subsonic case, the solution (48) is neither odd nor even. This is because of the logarithmic term that introduces the factor au in Eq. (44). This loss of parity is also expressed by the bow shock, which obviously breaks parity. This is related to the hyperbolic nature of the equation of motion (39), which distinguishes between the limits $\hat{z} \rightarrow \pm\infty$, as only the far upstream region $\hat{z} \rightarrow -\infty$ is associated with the initial condition of the Cauchy problem. Although the logarithmic term is expected from the free case described in Appendix A, we have seen above (47) that it is required to obtain a smooth solution upstream. Without this term, the regularity at $u = -1$ would imply $b \neq 0$ in (44), which would give an unphysical singularity on the upstream inverted Mach cone at $\theta = \pi - \theta_c$.

Two other differences from the subsonic case [116], where $v_{r1} = 0$ and $v_{\theta1} > 0$, are that we now have $v_{r1} < 0$ and $v_{\theta1} < 0$. Thus, whereas in the subsonic case the increased pressure due to the self-interactions was strong enough to slow down the flow as it moves closer to the BH (but remains at large distance), in the supersonic case the BH gravity is dominant and accelerates the dark matter fluid, with $v^2 > v_0^2$.

3. Second-order correction

The second-order correction $\hat{\beta}_1$, of order $1/\hat{r}$, is obtained by collecting the terms of order $1/\hat{r}^3$ in Eq. (34) and using the expression (48) for the first-order term $\hat{\beta}_0$. This gives the linear differential equation

$$\frac{\partial^2 \hat{\beta}_1}{\partial \hat{x}^2} + \frac{\partial^2 \hat{\beta}_1}{\partial \hat{y}^2} - \frac{1}{c_z^2} \frac{\partial^2 \hat{\beta}_1}{\partial \hat{z}^2} = \frac{1}{2\hat{\rho}_0 v_0 \hat{r}^3}. \quad (50)$$

In the upstream supersonic regime, the fields at a point \vec{r} only depend on the properties of the flow further upwind. In other words, we must solve Eq. (50) using the retarded propagator of the linear wave equation. Thus we write

$$\hat{\beta}_1 = \frac{c_z^2}{2\hat{\rho}_0 v_0} \int \frac{d\hat{x}' d\hat{y}' d\hat{z}'}{(\hat{r}'^2 + a^2)^{3/2}} \int \frac{dp_x dp_y d\omega}{(2\pi)^3}$$

$$\times \frac{e^{ip_x(\hat{x}-\hat{x}') + ip_y(\hat{y}-\hat{y}') - i\omega(\hat{z}-\hat{z}')}}{(\omega + i\epsilon)^2 - c_z^2(p_x^2 - p_y^2)}, \quad (51)$$

where $\epsilon \rightarrow 0^+$ and $a \rightarrow 0^+$. Here we used the Fourier-space expression of the retarded propagator, and we regularized the small-scale divergence of the source $1/\hat{r}^3$ with a smoothing cutoff $a > 0$, by replacing $1/\hat{r}^3 \rightarrow 1/(\hat{r}^2 + a^2)^{3/2}$. Performing the integrals and taking the limit $a \rightarrow 0^+$ we obtain

$$\hat{\beta}_1 = -\frac{c_z^2}{2\hat{\rho}_0 v_0 \hat{r}} \int_1^\infty \frac{dy}{(c_z^2 + y^2) \sqrt{\sin^2 \theta + y^2 \cos^2 \theta}}, \quad (52)$$

which behaves indeed as $1/\hat{r}$. This expression only applies to the half plane $\hat{z} < 0$. The integral (52) is even in \hat{z} (i.e. in u), but its first derivative is discontinuous at $u = 0$. This means that we must instead use the analytic continuation of (52) to extend this result to $u > 0$. Alternatively, we can go back to the differential equation (50) and substitute the ansatz

$$\hat{\beta}_1 = \frac{f_1(u)}{\hat{r}}, \quad (53)$$

which we know to be correct from the result (52), which ensures that there are no logarithmic corrections such as $\ln \hat{r}/\hat{r}$. This gives a second-order differential equation over f_1 ,

$$(1-u^2)[(1+c_z^2)u^2-1]f_1'' + u[5+3c_z^2-5(1+c_z^2)u^2]f_1'$$

$$+ (1+c_z^2)(1-3u^2)f_1 - \frac{1+c_z^2}{4v_0^3} = 0. \quad (54)$$

The two integration constants are set by the requirement that both $f_1(-1)$ and $f_1(-u_c)$ be finite. We finally obtain the expressions

$$-1 \leq u \leq -u_c:$$

$$f_1(u) = \frac{1+c_z^2}{8c_v^3 \sqrt{(1+c_z^2)u^2-1}}$$

$$\times \ln \left[\frac{1-(1+c_z^2)u - c_z \sqrt{(1+c_z^2)u^2-1}}{1-(1+c_z^2)u + c_z \sqrt{(1+c_z^2)u^2-1}} \right], \quad (55)$$

$$-u_c \leq u \leq u_c:$$

$$f_1(u) = -\frac{1+c_z^2}{4cv_0^3\sqrt{1-(1+c_z^2)u^2}} \times \left[\frac{\pi}{2} - \text{Arctan} \frac{1-(1+c_z^2)u}{c\sqrt{1-(1+c_z^2)u^2}} \right], \quad (56)$$

which agree with the integral expression (52). One can obtain Eq. (56) from Eq. (55) by using the property $\text{Arctan}(x) = \frac{i}{2} \ln \frac{1-ix}{1+ix}$. This provides the analytic continuation from $u < -u_c$ to $u > -u_c$. To derive Eq. (56) we also used the property $\text{Arctan}(1/x) = \pi/2 - \text{Arctan}(x)$ for $x > 0$, to obtain an expression that is regular at $u = 1/(1+c_z^2)$ (one needs to use the appropriate denomination of arctan to obtain an expression that is regular over the desired range of u). Near the shock, at $u \rightarrow u_c$, we obtain the Taylor expansion

$$u \rightarrow u_c^-: f_1(u) = -\frac{\pi(1+c_z^2)^{3/4}}{4\sqrt{2}cv_0^3\sqrt{u_c-u}} + \dots \quad (57)$$

The singularity at u_c , where the second-order velocities v_{r2} and $v_{\theta2}$ diverge, means that this perturbative approach breaks down near the shock, close to the downwind Mach cone.

As explained above, because of the hyperbolicity of the equations of motion in the supersonic regime, the solution in the upstream domain is fully determined by the local properties of the fluid (the sound speed c_s), the relative velocity v_0 and the long-range gravity of the BH. It is independent of the boundary conditions at the Schwarzschild radius and does not contain free integration constants.

C. Downstream region

1. First-order correction

In the far downstream region, we again have a large-distance expansion as in (35), with possible logarithmic factors $\ln(\hat{r})$.

The first-order upstream solution (48) is singular on the \hat{z} axis downstream, at $\theta = 0$ and $u = 1$. This is a signature of the fact that it does not apply downstream, for $\theta < \theta_s$, where $\theta_s(\hat{r})$ is the polar angle of the axisymmetric shock front at radius \hat{r} . The downstream solution still takes the general form (42), with $f_0^l(u)$ again of the form (44). The velocity potential $\hat{\beta}$ must be continuous across the shock. This implies that the term $a \ln \hat{r}$ is identical in the upstream and downstream functions, whence $a = -1/(2v_0)$ again. The solution must now be regular at $u = 1$, which determines b , while the second integration constant for f_0 is set by the continuity at $u = u_c$. This gives

$$\hat{\beta}_0 = -\frac{1}{2v_0} \ln \hat{r} + f_0(u), \quad (58)$$

with

$$f_0(u) = -\frac{\ln(1+u)}{2v_0} + \frac{1}{2v_0} \times \ln \left[\frac{1+(1+c_z^2)u - c_z\sqrt{(1+c_z^2)u^2-1}}{-1+(1+c_z^2)u + c_z\sqrt{(1+c_z^2)u^2-1}} \right], \quad (59)$$

and we obtain

$$\begin{aligned} v_{r1} &= -\frac{1}{2v_0\hat{r}}, \\ v_{\theta1} &= \frac{-1}{2v_0\hat{r}\sqrt{1-u^2}} \left[1+u - \frac{2c_z}{\sqrt{u^2/u_c^2-1}} \right], \\ v_1^2 &= \frac{1}{\hat{r}} - \frac{2c_z}{\hat{r}\sqrt{u^2/u_c^2-1}}, \\ \hat{\rho}_1 &= \frac{2c_z}{\hat{r}\sqrt{u^2/u_c^2-1}}. \end{aligned} \quad (60)$$

Thus, we can see that the scalar-field density is increased behind the shock, by an amount that decreases at large distance as $1/\hat{r}$, whereas the upstream density (49) was not modified at this order. The radial velocity is continuous through the shock. This is consistent with the continuity of $\hat{\beta}$ for a shock that has a fixed direction θ_s at leading order at large distance.

The jump conditions for an isentropic potential flow across a shock are different from the Rankine-Hugoniot jump conditions that apply to the Navier-Stokes equations (e.g. there is no energy equation and no entropy in our system); see hydrodynamics textbooks such as [130]. The jump conditions are the continuity of the velocity potential $\hat{\beta}$, which also implies the continuity of the tangential velocity v_t , and the continuity of the transverse mass flow $\hat{\rho}v_n$, where v_n is the normal velocity. In our case, at large distance we have $v_t = v_r$ and $v_n = v_\theta$ at leading order. Thus, we recover the continuity of v_r at this order, whereas the condition of continuity of $\hat{\rho}v_\theta$ at order $1/\hat{r}$ gives the angle of the shock,

$$\hat{r} \rightarrow \infty: \theta_s \rightarrow \theta_c, \quad (61)$$

where θ_c was defined in Eq. (45). Thus, as expected, at large distance the shock follows the Mach cone.

We can see that the first-order angular velocity $v_{\theta1}$ and density $\hat{\rho}_1$ of Eq. (60) diverge at u_c , that is, on the downwind Mach cone, as the function $f_0(u)$ has the expansion

$$u \rightarrow u_c^+ : f_0(u) = -\frac{\ln(1-u_c)}{2v_0} - \frac{\sqrt{2}(1+c_z^2)^{3/4}}{c_z v_0} \sqrt{u-u_c} + \dots \quad (62)$$

This signals that the perturbative analysis presented above breaks down close to the shock, and we must take into account nonlinear effects in a boundary layer just behind the shock. This singularity appears at the first order f_0 , whereas in the upstream case it only appeared at the second order f_1 , in Eq. (57).

2. Second-order corrections

As we shall see in Sec. III D below, the matching conditions along the boundary layers and the shock generate logarithmic contributions that impact the downstream bulk flow. Therefore, as compared with the upstream expression (53) the second-order expression of the

downstream velocity potential contains an additional logarithmic term,

$$\hat{\beta}_1 = \frac{f_1(u) + g_1(u) \ln \hat{r}}{\hat{r}}. \quad (63)$$

Substituting this expression into the equation of motion (34), with the result (59) for the first order, and collecting terms of order $1/\hat{r}^3$ and $\ln \hat{r}/\hat{r}^3$ give two coupled linear second-order differential equations over f_1 and g_1 . Regularity at $u = 1$ determines an integration constant for each of these two functions, and we obtain

$$g_1 = \frac{C_2}{\sqrt{(1+c_z^2)u^2-1}}, \quad (64)$$

and

$$f_1 = -\frac{3(1+c_z^2)^2 u}{2v_0^3[(1+c_z^2)u^2-1]} + \frac{1}{\sqrt{(1+c_z^2)u^2-1}} \left\{ C_1 + \frac{C_2}{2} \ln \left[\frac{[(1+c_z^2)u^2-1]^2[1+(1+c_z^2)u-c_z\sqrt{(1+c_z^2)u^2-1}]}{(1+u)^2[-1+(1+c_z^2)u+c_z\sqrt{(1+c_z^2)u^2-1}]} \right] \right. \\ \left. + \frac{1+c_z^2}{4c_z v_0^3} \ln \left[\frac{(1+u)^3[-1+(1+c_z^2)u+c_z\sqrt{(1+c_z^2)u^2-1}]^4}{[(1+c_z^2)u^2-1]^2[1+(1+c_z^2)u-c_z\sqrt{(1+c_z^2)u^2-1}]^3} \right] + \frac{(1+c_z^2)^{3/2}}{2c_z v_0^3} \ln \left[\frac{\sqrt{1+c_z^2}u+1}{\sqrt{1+c_z^2}u-1} \right] \right\}, \quad (65)$$

where C_1 and C_2 are the two remaining integration constants.

D. Shock front and boundary layers

1. Large-distance expansions

We have seen above that the large-distance expansions of the upstream and downstream bulk flows diverge at $u \rightarrow u_c$. Then, close to u_c the first- or second-order velocity corrections become greater than the zeroth-order velocity v_0 , and the large-distance expansion (35) breaks down. Therefore, on both sides of the shock a boundary layer appears, where nonlinearities play a key role and we need to go beyond the expansion (35).

As described in Appendix B, a careful analysis shows that the boundary layers have a width $\Delta u \sim \hat{r}^{-2/3}$. This implies that we need to introduce expansions over powers of $\hat{r}^{-1/3}$ and not only of \hat{r}^{-1} . Moreover, there are again logarithmic contributions. To start with, we need to specify the location $\theta_s(\hat{r})$ of the shock front, which we write as the large-distance expansion

$$\theta_s(\hat{r}) = \theta_c + \frac{\theta_1}{\hat{r}^{2/3}} + \frac{\theta_2 + \psi_2 \ln \hat{r}}{\hat{r}} + \frac{\theta_3 + \psi_3 \ln \hat{r}}{\hat{r}^{4/3}} + \dots \quad (66)$$

This defines in turn the expansion of $u_s(\hat{r}) = \cos[\theta_s(\hat{r})]$. The zeroth-order terms θ_c and u_c , defined in Eqs. (45)

and (46), were derived in Eq. (61) from the matching of the first-order upstream and downstream bulk flows $\hat{\beta}_0$.

Because the width of the boundary layer is of order $\hat{r}^{-2/3}$, we introduce the boundary-layer coordinate

$$U = \hat{r}^{2/3}[u - u_s(\hat{r})]. \quad (67)$$

We can see from Eq. (57) that the upstream bulk flow diverges as $v_\theta \sim \hat{r}^{-2}(u_c - u)^{-3/2}$, whereas from Eq. (62) the downstream bulk flow diverges as $v_\theta \sim \hat{r}^{-1}(u - u_c)^{-1/2}$. Thus, the singularity close to the shock appears at a lower order in $1/\hat{r}$ on the downstream side. This asymmetry means that whereas for the upstream boundary layer (i.e. just before the shock) we have the expansion

$$U < 0 : \hat{\beta} = v_0 \hat{r} u - \frac{1}{2v_0} \ln[\hat{r}(1-u)] + \frac{F_2(U)}{\hat{r}^{2/3}} + \frac{F_3(U)}{\hat{r}} + \dots, \quad (68)$$

for the downstream boundary layer (i.e. just after the shock) we have

$$U > 0 : \hat{\beta} = v_0 \hat{r} u - \frac{1}{2v_0} \ln[\hat{r}(1-u_c)] + \frac{F_1(U)}{\hat{r}^{1/3}} + \frac{F_2(U)}{\hat{r}^{2/3}} + \frac{F_3(U) + \mathcal{F}_3(U) \ln \hat{r}}{\hat{r}} + \dots \quad (69)$$

In both cases we keep the regular part over u of the bulk flow, up to the order where the expansion over $1/\hat{r}$ breaks down. In the upstream case (68), this corresponds to the first two terms of order \hat{r} and \hat{r}^0 , whereas in the more singular downstream case (69) this corresponds to the first term only, of order \hat{r} (and to the constant associated with the second term). This implies that whereas the boundary-layer expansion in U starts at order $\hat{r}^{-2/3}$ in the upstream case, it starts earlier at order $\hat{r}^{-1/3}$ in the downstream case. One can check that there are no logarithmic terms $\ln \hat{r}$ in the upstream boundary layer, as there was no logarithmic term either in the upstream second-order bulk flow (53). However, logarithmic terms appear through nonlinear effects in both the shock curve (66) and the downstream boundary layer (69).

As compared with standard one-dimensional boundary-layer theory [131], $\hat{r}^{-1/3}$ plays the role of the small parameter, and U is the boundary-layer coordinate that is stretched to account for its infinitesimal width $\Delta u \sim \hat{r}^{-2/3}$.

In Secs. V and VI we will compute the accretion rate onto the BH and its dynamical friction. This involves surface integrals on a sphere of radius R , where we take the limit $R \rightarrow \infty$ to use the large-distance expansions described above. These integrals give rise to a geometrical area prefactor \hat{r}^2 . This implies that we must compute velocity and density fields up to order $1/\hat{r}^2$, to obtain the constant term that determines the accretion rate and the dynamical friction. This corresponds to the term of order $1/\hat{r}$ in the velocity potential $\hat{\beta}$. This is why we need to go to order $1/\hat{r}$ in the bulk flows (35) and in the boundary layers (68) and (69).

2. Order θ_1 and F_1

We simultaneously compute the boundary-layer expansions and the shock front order by order in $\hat{r}^{-1/3}$. At zeroth order, there are no boundary layers, and we extend the upstream and downstream bulk flows $\hat{\beta}_0$ up to the shock front. As found in Eq. (61), the matching condition on the shock front also determines the zeroth-order term θ_c in the shock expansion (66).

The next order is associated with the term $\theta_1/\hat{r}^{2/3}$ in the shock expansion (66) and with the terms $F_1/\hat{r}^{1/3}$ in the boundary-layer expansions (68) and (69). We can see that the term F_1 is absent in the upstream boundary layer. As noticed above, this is because the singularity of the upstream bulk flow appears at a higher order in $1/\hat{r}$ than for the downstream bulk flow. Therefore, at this order, we truncate the shock expansion (66) at the term $\theta_1/\hat{r}^{2/3}$, the upstream bulk flow obtained in Sec. III B extends down to the shock θ_s , and there is only one boundary layer behind the shock, given by the expansion (69) truncated at the term $F_1/\hat{r}^{1/3}$.

The upstream bulk flow, given by Eqs. (47) and (56), provides the boundary conditions on the shock, at the angular location θ_s , that is, at $U = 0$. Then, using the

downstream boundary-layer expression (69), the continuity of the velocity potential $\hat{\beta}$ and of the normal momentum $\hat{p}_n = \hat{\rho}v_n$ give

$$F_1(0) = 0, \quad F_1'(0) = -\frac{4v_0\theta_1}{9c_z^2}. \quad (70)$$

Next, substituting the expansion (69) in the equation of motion (34) and collecting the terms of order $\hat{r}^{-5/3}$, we obtain the differential equation

$$\left(U - \frac{c_z\theta_1}{\sqrt{1+c_z^2}}\right)F_1'' + \frac{1}{2}\left(1 - \frac{9c_z^2}{v_0\sqrt{1+c_z^2}}F_1'\right)F_1' = 0. \quad (71)$$

This differential equation is nonlinear, which shows the importance of nonlinear effects in the boundary layer that were not captured by the perturbative treatment in Sec. III C 1. The solution can be expressed by the parametric representation in terms of the auxiliary variable Y ,

$$\begin{aligned} U &= \frac{c_z\theta_1}{\sqrt{1+c_z^2}} + \frac{16v_0^3\theta_1^3 - 729c_z^3Y^3}{243v_0c_z\sqrt{1+c_z^2}Y^2}, \\ F_1 &= \frac{-64v_0^3\theta_1^3 + 729c_z^3Y^3}{486v_0c_z\sqrt{1+c_z^2}Y}, \\ &\text{with } 0 < Y < \frac{4v_0\theta_1}{9c_z}, \quad 0 < U < \infty, \end{aligned} \quad (72)$$

where we used the boundary conditions (70) to determine two integration constants.

Next, we write the expansion of this result at large U , in powers of $1/U$, in the rear of the boundary layer. Expressed next in terms of u , this gives the expansion

$$\begin{aligned} \hat{\beta} &= \hat{r}v_0u + \left[-\frac{\ln[\hat{r}(1-u_c)]}{2v_0} - \frac{8v_0\theta_1^{3/2}\sqrt{u-u_c}}{3^{5/2}c_z^{1/2}(1+c_z^2)^{1/4}} + \dots \right] \\ &+ \hat{r}^{-1} \left[-\frac{8c_zv_0\theta_1^3}{81(1+c_z^2)} \frac{1}{u-u_c} + \dots \right] + \dots \end{aligned} \quad (73)$$

The dots in the brackets correspond to higher orders in $u - u_c$ that are generated by higher orders in the boundary-layer expansion (69) (the functions F_2, F_3, \dots) while the dots at the end correspond to higher orders in $1/\hat{r}$.

This must be matched to the expansion of the bulk downstream flow (59)–(65) at $u \rightarrow u_c^+$,

$$\begin{aligned} \hat{\beta} &= \hat{r}v_0u + \left[-\frac{\ln[\hat{r}(1-u_c)]}{2v_0} - \frac{\sqrt{2}(1+c_z^2)^{3/4}\sqrt{u-u_c}}{v_0c_z} + \dots \right] \\ &+ \hat{r}^{-1} \left[-\frac{3(1+c_z^2)}{4v_0^3} \frac{1}{u-u_c} + \dots \right] + \dots \end{aligned} \quad (74)$$

Both terms in θ_1 in Eq. (73) match those in Eq. (74) for

$$\theta_1 = \left(\frac{3}{2}\right)^{5/3} \frac{(1 + c_z^2)^{2/3}}{v_0^{4/3} c_z^{1/3}}. \quad (75)$$

This determines the coefficient θ_1 and the location of the shock (66) at this order. The fact that we can simultaneously match both θ_1 terms in Eq. (73) provides a check of the computation. This asymptotic matching procedure, where we match the large- U behavior of the boundary layer with the small $u - u_c$ behavior of the downstream bulk flow (i.e., the rear of the boundary layer with the behavior of the bulk flow close to the shock), allows us to obtain the global solution over all space.

The width $\hat{r}^{-2/3}$ of the boundary layer is found from Eq. (71). This is the scaling that ensures the balance between the linear and nonlinear terms in Eq. (71), as powers of \hat{r} cancel out. This is explained in more detail in Appendix B. The regularization of the divergences at the shock found in the perturbative treatment of the bulk flow in Sec. III C is made possible by this nonlinearity.

3. Higher orders F_2 and F_3

We use the same method to compute the shock and the boundary layers at orders $\{\theta_2, \psi_2; F_2\}$ and $\{\theta_3, \psi_3; F_3, \mathcal{F}_3\}$. The additional ingredient is that we now have two boundary layers. The functional form of F_2, F_3, \mathcal{F}_3 is again obtained by substituting into the equation of motion (34), while the integration constants are determined by the junction conditions. We now have two asymptotic matchings, between the rear of each boundary layer and the bulk flow, and simple junction conditions between both boundary layers on the shock. A detailed computation shows that we need to introduce the logarithmic terms in the expansions (66) and (69) to satisfy these junction conditions. Then, this fully determines ψ_2 in the shock expansion (66) and the integration constant C_2 in the bulk downstream solution (64) and (65), while the integration constant C_1 in Eq. (65) is expressed in terms of θ_2 , which remains undetermined. We do not give the expressions of these higher-order results here, as they are somewhat lengthy and not especially illuminating.

4. Shock front

From the analytical solution derived in the previous sections, we obtain the discontinuity of the density and velocity across the shock,

$$\begin{aligned} \Delta\hat{\rho} &= \frac{2^{4/3} c_z^{2/3} v_0^{2/3}}{3^{1/3} (1 + c_z^2)^{1/3} \hat{r}^{2/3}} \frac{1}{\hat{r}^{2/3}} + \dots \\ \Delta v_r &= \frac{3^{1/3} (1 + c_z^2)^{5/6}}{2^{1/3} c_z^{2/3} v_0^{5/3}} \frac{1}{\hat{r}^{4/3}} + \dots \\ \Delta v_\theta &= \frac{2^{1/3} (1 + c_z^2)^{1/6}}{3^{1/3} c_z^{1/3} v_0^{1/3}} \frac{1}{\hat{r}^{2/3}} + \dots \end{aligned} \quad (76)$$

The discontinuity of the radial velocity appears at a higher order over $1/\hat{r}$ because at large distance the radial velocity is parallel to the shock front and conserved at leading order. Going back to dimensional units, this gives the large-distance scalings

$$\begin{aligned} \Delta\rho &\sim \left(\frac{r}{r_{\text{sg}}}\right)^{-2/3} \rho_0, \\ \Delta v_\theta &\sim \left(\frac{r}{r_{\text{sg}}}\right)^{-2/3} \mathcal{M}_0^{-1} v_0 = \left(\frac{r}{r_{\text{sg}}}\right)^{-2/3} c_s. \end{aligned} \quad (77)$$

IV. DRAG FORCE ON THE BH

A. Relation between the accretion rate and the large-distance expansion

As explained above, at the order that we need in this paper, we now have the global solution of the flow at large distance, except for an unknown parameter θ_2 , defined from the expansion (66) of the shock, or equivalently an integration constant in the downstream solution. This remaining freedom is due to the fact that so far we have not used the inner boundary condition close to the BH. In fact, this parameter will simply be determined by the accretion rate onto the BH, which is thus sufficient to describe the boundary condition at the Schwarzschild radius.

In the steady state, the accretion rate onto the BH is given by the flux of matter through any closed surface that surrounds the BH. Choosing a sphere of radius \hat{r} , the accretion rate writes as

$$\dot{M}_{\text{BH}} = -2\pi\hat{r}^2 \int_{-1}^1 du \hat{\rho} v_r. \quad (78)$$

Thus, we can relate \dot{M}_{BH} to the large-distance expansion by computing the radial momentum $\hat{\rho} v_r$ up to order $1/\hat{r}^2$. To handle the fact that we have obtained separate expressions for the scalar field profile over four domains, the upstream and downstream bulk flows and the boundary layers, with two asymptotic matchings in between, we define the angular function

$$\dot{M}_{\text{BH}}(u) = -2\pi\hat{r}^2 \int_{-1}^u du \hat{\rho} v_r, \quad (79)$$

so that the total accretion rate is $\dot{M}_{\text{BH}}(u = 1)$. Then, up to integration constants, we obtain $\dot{M}_{\text{BH}}(u)$ in each domain from the appropriate expression of the scalar-field flow. Next, as for the flow, the integration constants are determined by the two asymptotic matchings at the rear of the two boundary layers and by continuity at the shock location. This determines the global function $\dot{M}_{\text{BH}}(u)$ and the total accretion rate $\dot{M}_{\text{BH}}(1)$. We obtain

$$\begin{aligned} \dot{M}_{\text{BH}} = & -\frac{4\pi c_z v_0 \theta_2}{\sqrt{1+c_z^2}} - \frac{\pi(20+12c_z^2+\sqrt{3}\pi)}{3v_0} \\ & - \frac{4\pi\sqrt{1+c_z^2}}{3v_0} \ln \left[\frac{16(\sqrt{1+c_z^2}-1)^3 v_0^2}{3c_z^4(1+c_z^2)} \right] \\ & - \frac{2\pi}{9v_0} \ln \left[\frac{(\sqrt{1+c_z^2}-1)^{18} v_0^{16}}{2^{16} 3^8 c_z^{20} (1+c_z^2)^{11}} \right]. \end{aligned} \quad (80)$$

As expected, we can see that the result (80) does not depend on the radius \hat{r} . All terms with higher powers of \hat{r} eventually cancel out, and the large-radius limit, $\hat{r} \rightarrow \infty$, gives a finite result. This agrees with the fact that the matter flux does not depend on the choice of the surface enclosing the BH, in the stationary regime.

As announced above, the expression (80) relates the remaining large-distance unknown parameter θ_2 to the accretion rate \dot{M}_{BH} . By construction the large-distance expansion cannot know about the inner boundary condition (which is beyond its domain of validity) and cannot determine the accretion rate \dot{M}_{BH} . However, the flow at large distance remains sensitive to the accretion rate because of the constant-flux condition in the steady state, as explicitly shown by Eq. (80).

B. Accretion drag and dynamical friction

In [116], using the Euler equation associated with the Bernoulli equation (31), we showed that the drag force on the BH can be written as

$$\hat{F}_z = -2\pi\hat{r}^2 \int_{-1}^1 du (\hat{\rho} v_r v_z + \hat{P}u), \quad (81)$$

where we have chosen the surface of integration to be a sphere of radius \hat{r} . As for the accretion rate in Eq. (79), we define a function $\hat{F}_z(u)$ to compute the drag force in each angular domain, up to integration constants. The junction conditions and asymptotic matching then provide the global function, and the full dynamical friction is obtained from $\hat{F}_z(u=1)$. Using Eq. (80) to express θ_2 in terms of \dot{M}_{BH} , we obtain

$$\hat{F}_z = \dot{M}_{\text{BH}} v_0 + \frac{2\pi c_z^2}{3(1+c_z^2)} \ln \left[\frac{e v_0^4 c_z \hat{r}^2}{18(1+c_z^2)^2} \right], \quad (82)$$

where $e = \exp(1)$ is the base of the natural logarithm. In dimensional units, this reads as

$$F_z = \dot{M}_{\text{BH}} v_0 + \frac{\pi}{3} \rho_a r_s^2 \frac{c_{s0}^2}{v_0^2} \ln \left[\frac{e v_0^4 c_z r^2}{18(1+c_z^2)^2 r_s^2} \right]. \quad (83)$$

Thus, our computation recovers in a unified manner two contributions to the total drag force,

$$F_z = F_{\text{acc}} + F_{\text{df}}, \quad (84)$$

where the first term is directly related to the accretion of matter, and therefore of momentum, by the BH, whereas the second term is the classical dynamical friction, associated with the long-range gravitational attraction from the wake behind the BH when pressure forces are present.

V. TWO REGIMES FOR THE BH ACCRETION RATE

As explained above, we must derive \dot{M}_{BH} by other methods than the large-distance expansion, so as to handle the boundary condition at the horizon. This requires a fully relativistic treatment. We do not perform such a numerical computation of the axisymmetric relativistic flow down to the horizon in this paper, but we present a simple approximation that should capture the main behaviors.

A. Self-regulated accretion at moderate Mach numbers

As recalled in Sec. II E, in the radial case the accretion rate is given by the expression (29). We showed in [116] that this accretion rate remains valid in the subsonic regime, up to $v_0 \lesssim c_{s0}$. Indeed, below the transition radius $r_{\text{sg}} \gg r_s$, the flow quickly becomes approximately radial, and one recovers the radial solution. This accretion rate is much smaller than the spherical Bondi accretion rate [125], $\dot{M}_{\text{Bondi}} \sim \rho_0 r_s^2 / c_{s0}^3$, because of the steep effective adiabatic index $\gamma = 2$. In the supersonic regime, one usually expects to recover the Hoyle-Lyttleton accretion rate [132,133]

$$\dot{M}_{\text{HL}} = \frac{4\pi\rho_0\mathcal{G}^2 M_{\text{BH}}^2}{v_0^3} = \frac{\pi\rho_0 r_s^2}{v_0^3}. \quad (85)$$

However, for moderate Mach numbers this accretion rate is of the order of the Bondi prediction and still much higher than the radial accretion rate (29). The latter is the highest possible flux (for radial symmetry) allowed by the effective pressure associated with the self-interactions [95]. Lower accretion rates are associated with solutions that are fully subsonic (which is not physical because of the boundary condition at the BH horizon) or fully supersonic. Therefore, in the regime $\dot{M}_{\text{HL}} > \dot{M}_{\text{BH,radial}}$ a bow shock appears that slows down and deflects the dark matter and allows the matching to the boundary conditions at the BH horizon with their much smaller accretion rate. This creates a subsonic region behind the shock and around the BH, where the flow becomes approximately radial close to the BH horizon and matches the accretion rate (29). We shall present in Sec. VIII below numerical computations that confirm this behavior. In a sense, because the maximum possible accretion rate (29) is much smaller than the incoming flow (85), the BH (dressed by the surrounding scalar cloud with large self-interactions) acts like an

obstacle, such as a solid sphere moving in a fluid or a space shuttle in the atmosphere.

B. Bondi-Hoyle-Lyttleton accretion at high Mach numbers

At high velocities, $v_0^3 > c_{s0}^2/(3F_\star)$, the Hoyle-Lyttleton accretion rate (85) becomes smaller than the value (29), associated with the highest possible flux. This means that matter can directly fall into the BH along a fully supersonic solution. Thus, the BH is no longer an obstacle but a sink where matter can freely fall. However, on the z axis behind the BH, there is still a wake and a conical shock as streamlines coming from all directions converge toward the symmetry axis but cannot cross. There is also a stagnation point on the z axis behind the BH, where the velocity vanishes, because the radial velocity must be negative and of the order of the speed of light close to the horizon and positive and close to v_0 at large radii. This turning point separates the streamlines that fall into the BH and those that escape to infinity. Clearly this region is subsonic; therefore we always have a subsonic region behind the BH. Thus, we can expect that for high velocities the shock becomes attached to the BH, with an upstream supersonic regime that extends down to the horizon on the front side of the BH and a narrow shock cone on the back side that contains a subsonic region. This agrees with the accretion column of the Hoyle-Lyttleton analysis [132,133]. We discuss in more detail this regime in Appendix C. We find that pressure forces do not modify the main properties of the Hoyle-Lyttleton accretion and for $v_0 > c_{s0}^{2/3}$ we have a narrow accretion column on the rear side of the BH.

Therefore, we have the moderate and high-velocity behaviors

$$v_0 < \frac{c_{s0}^{2/3}}{(3F_\star)^{1/3}} : \dot{M}_{\text{BH}} = \frac{12\pi F_\star \rho_0 \mathcal{G}^2 M_{\text{BH}}^2}{c_{s0}^2}, \quad (86)$$

$$v_0 > \frac{c_{s0}^{2/3}}{(3F_\star)^{1/3}} : \dot{M}_{\text{BH}} = \frac{4\pi \rho_0 \mathcal{G}^2 M_{\text{BH}}^2}{v_0^3}, \quad (87)$$

which we will use in the following.

VI. COMPARISON OF ACCRETION DRAG AND DYNAMICAL FRICTION

A. Accretion drag

From Eqs. (83) and (86) and (87), the accretion drag on the BH shows the low- and high-velocity behaviors

$$v_0 < \frac{c_{s0}^{2/3}}{(3F_\star)^{1/3}} : F_{\text{acc}} = \frac{12\pi F_\star \rho_0 \mathcal{G}^2 M_{\text{BH}}^2 v_0}{c_{s0}^2}, \quad (88)$$

$$v_0 > \frac{c_{s0}^{2/3}}{(3F_\star)^{1/3}} : F_{\text{acc}} = \frac{4\pi \rho_0 \mathcal{G}^2 M_{\text{BH}}^2}{v_0^2}. \quad (89)$$

B. Dynamical friction

For $v_0 \gtrsim c_{s0}$ the dynamical friction term in (83) reads as

$$F_{\text{df}} = \frac{8\pi \rho_0 \mathcal{G}^2 M_{\text{BH}}^2}{3v_0^2} \ln\left(\frac{r_a}{r_{\text{UV}}}\right), \quad (90)$$

with

$$r_{\text{UV}} \simeq \sqrt{\frac{18}{e}} r_{\text{sg}} \mathcal{M}_0^{-3/2} = \sqrt{\frac{18}{e}} r_s v_0^{-3/2} c_{s0}^{-1/2}. \quad (91)$$

The effective small-scale cutoff r_{UV} is explicitly obtained from the analytical computation (83). Thus, the pressure associated with the self-interactions damps the contributions from small scales to the dynamical friction and in contrast with the collisionless result the Coulomb logarithm does not show a small-scale divergence. On the other hand, we still have a large-scale logarithmic divergence, as for the seminal computation by Chandrasekhar for a stellar cloud [114]. One often takes this large-scale cutoff to be the size of the cloud. In our case, this is not a free parameter as it is given by the soliton radius $R_{\text{sol}} = \pi r_a$ defined in Eq. (25).

We can check that the radius r_{UV} is always greater than the Schwarzschild radius as v_0 and c_{s0} are smaller than the speed of light. The comparison with Eq. (77) shows that the radius r_{UV} is the radius where the velocity is significantly perturbed by the shock, with a relative discontinuity $\Delta v_\theta/v_0$ of order unity. As compared with the free collisionless case, this explains the origin of the small-scale cutoff in the Coulomb logarithm and why smaller radii do not contribute significantly to the dynamical friction.

Thus, we find that the accretion drag is negligible at low velocity but of the same order as the dynamical friction at high velocity,

$$\begin{aligned} v_0 &\ll \frac{c_{s0}^{2/3}}{(3F_\star)^{1/3}} : F_{\text{acc}} \ll F_{\text{df}}, \\ v_0 &> \frac{c_{s0}^{2/3}}{(3F_\star)^{1/3}} : F_{\text{acc}} \sim F_{\text{df}}, \end{aligned} \quad (92)$$

where we used Eqs. (86) and (87), as also discussed in Appendix C.

VII. GRAVITATIONAL FORCE FROM THE LARGE-DISTANCE BH WAKE

The dynamical friction is often estimated from the gravitational force exerted on the moving object by the overdensity created in its wake. For collisionless systems, this was shown to give back the classical Chandrasekhar result that was obtained from the deflection of distant

orbits [134]. In our case, this neglects pressure effects, but it should provide at least a correct order of magnitude at high wave numbers. We focus on the high Mach number regime, where the Mach angle is small and the accretion proceeds through the accretion column at the rear of the BH, as detailed in Appendix C. Then, considering a conical accretion column of Mach angle $\theta_c \ll 1$ at large distance, its gravitational drag force on the BH reads as

$$F_g = \mathcal{G}M_{\text{BH}} \int dr \pi (r\theta_c)^2 \frac{\rho - \rho_0}{r^2} \quad (93)$$

$$= \mathcal{G}M_{\text{BH}} \pi \theta_c^2 \int dr (\rho - \rho_0), \quad (94)$$

where ρ is the typical density inside the column at distance r . Let us estimate the contribution from large radii, beyond the Hoyle-Lyttleton radius (C10), where the shock is weak. Upstream of the shock, pressure effects are small, and the streamlines follow the Keplerian orbits and density (C1)–(C3). At first order over θ_c and $1/r$, we obtain at large distance

$$\begin{aligned} r &= \frac{b}{\theta_c} - \frac{2\mathcal{G}M_{\text{BH}}}{v_0\theta_c^2}, & v_r &= v_0 - \frac{\mathcal{G}M_{\text{BH}}}{v_0 r}, \\ v_\theta &= -v_0\theta_c - \frac{2\mathcal{G}M_{\text{BH}}}{v_0\theta_c r}, & \rho &= \rho_0. \end{aligned} \quad (95)$$

As expected, we find that upstream of the shock, there is no modification of the density at order $1/r$; see Eq. (49). These expressions provide the boundary conditions $\{v_{r_1}, v_{\theta_1}, \rho_1\}$ upstream of the shock. The junction conditions are the continuity of the longitudinal velocity v_r and of the transverse momentum ρv_θ , while the Bernoulli equation (C8) remains satisfied. Writing $\rho_2 = \rho_1 + \Delta\rho$ and $v_{\theta_2} = v_{\theta_1} + \Delta v_\theta$, going up to second order over $\Delta\rho$ and Δv_θ , we obtain the solution

$$\Delta v_\theta = \frac{8\mathcal{G}M_{\text{BH}}}{3c_{s0}r}, \quad \Delta\rho = \rho_0 \frac{8\mathcal{G}M_{\text{BH}}}{3c_{s0}^2 r}, \quad (96)$$

where we used $\theta_c = c_{s0}/v_0$ at first order. Substituting $\rho - \rho_0 = \Delta\rho$ in Eq. (94), we obtain

$$F_g = \frac{8\pi\rho_0\mathcal{G}^2 M_{\text{BH}}^2}{3v_0^2} \int \frac{dr}{r}. \quad (97)$$

Thus, we recover the exact expression (90), with the Coulomb logarithm and the prefactor $8\pi/3$, which differs from the standard collisionless result 4π by a factor of $2/3$. Of course, this computation cannot compute the small-scale cutoff r_{UV} of Eq. (91).

The result (97) neglects the boundary layers and applies the junction conditions at the shock between the upstream and downstream bulk flows. Thus, we found in (77) that along the shock the density jump actually decays as $r^{-2/3}$

instead of r^{-1} . However, the width of the boundary layer also decreases as $\Delta u \sim r^{-2/3}$, which gives an angular width $\Delta\theta \sim r^{-2/3}$. Therefore, the contribution from the boundary layer to the gravitational force takes the form

$$F_{g,\text{bl}} \sim \mathcal{G}M_{\text{BH}} \int dr 2\pi (r\theta_c) r \Delta\theta \frac{\Delta\rho}{r^2} \propto \int dr r^{-4/3}. \quad (98)$$

Thus, this contribution is finite and does not show a large-distance logarithmic divergence. It is therefore subdominant at large distance. This is why the simple computation (97) can recover the exact large-distance behavior of the dynamical friction (90).

VIII. NUMERICAL COMPUTATION AT MODERATE MACH NUMBER

To confirm the behavior of the system for moderate Mach numbers, we perform a numerical computation of the scalar dark matter flow around the BH using the public AMRVAC code [135–137]. This is a parallel adaptive mesh refinement framework aimed at solving partial differential equations for use in computational hydrodynamics and astrophysics. Similar studies for the Bondi-Hoyle accretion of a polytropic gas have been presented in [138,139], using also the AMRVAC code. They consider a polytropic gas of index $\gamma = 5/3$. As compared with our case, they also need to supplement the continuity and Euler equations with the energy equation, as the entropy is not conserved at the shock. In contrast, we do not need this energy equation because our fluid is not a perfect gas but a scalar field. In particular, the velocity is always curl-free as it is defined as the gradient of the phase β , which is the original field of interest, with the amplitude $\sqrt{\rho}$ of the wave function ψ .

Thus, we solve the continuity and Euler equations of an isentropic polytropic gas of index $\gamma = 2$, from the mapping described in Sec. II F in the nonrelativistic regime. The boundary condition at large radii is set by the uniform flow at density ρ_0 and velocity \vec{v}_0 . The boundary condition at the inner matching radius r_m is set by the radial solution (29). For the initial condition, we take for the density $\rho = \rho_0 \max(1, r_{\text{sg}}/(2r))$, which is an approximation of the radial solution [95]. For the initial velocity we take $v_r = -\dot{M}_{\text{B}}/(4\pi\rho r^2) + v_0 \cos\theta$ and $v_\theta = -v_0 \sin\theta$, that is, a simple combination of the uniform flow \vec{v}_0 with the radial infall. Then, we solve the dynamics over time until the results converge to a steady state.

We use a two-dimensional spherical mesh (thanks to the axisymmetry there is no dependence on the azimuthal angle φ), with a uniform stretching in the radial direction. The upper radius is taken at $50r_{\text{sg}}$ and the lower radius at $0.005r_{\text{sg}}$. We use a temporally first-order scheme, as we are only interested in a steady state, and the HLLC flux scheme [140]. We use the dimensionless coordinates and fields $r/r_{\text{sg}}, \rho/\rho_0, v/c_{s0}$, to work with quantities of order unity in

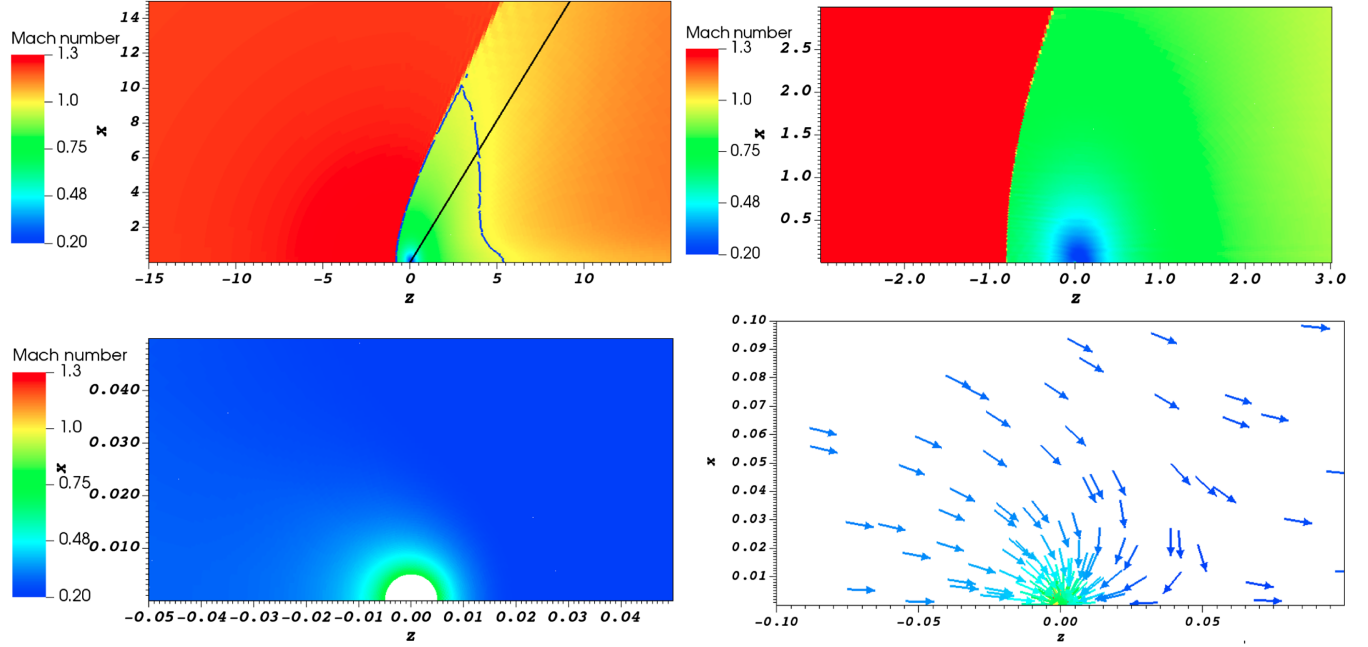


FIG. 1. Numerical computation of the scalar dark matter flow around a BH, as viewed in the BH frame with the dark matter coming from the left at the uniform velocity \vec{v}_0 parallel to the horizontal axis. We take $\mathcal{M}_0 = v_0/c_{s0} = 1.2$ and $c_{s0} = 0.05$. The coordinates are in units of the transition radius r_{sg} . The upper and bottom-left panels show maps of the Mach number $\mathcal{M} = v/c_s$ as we enlarge closer to the BH. The lower-right panel shows a map of the velocity field.

the transition region. We checked that the Bernoulli invariant (31) is constant throughout the computational domain.

We show our results in Fig. 1 for the case $v_0/c_{s0} = 1.2$ and $c_{s0} = 0.05$. We use the visualization tool VisIt [141,142]. The maps of the local Mach number \mathcal{M} in the upper panels clearly show the formation of a bow shock, upstream of the BH at a distance $r \simeq 0.8r_{\text{sg}}$ along the z axis. After the shock, the velocity decreases while the density and the local sound speed increase, which gives a clear drop of the Mach number $\mathcal{M} = v/c_s$. This is much more apparent than in the density maps, which are dominated by the radial increase close to the BH. The Mach number first keeps decreasing closer to the BH, until a radius $0.2r_{\text{sg}}$, and next increases as we move closer to the supersonic regime, which is beyond the computational domain. Indeed, as seen by the lower left panel, the Mach number has not reached unity at the inner radius of the grid, because we impose the boundary conditions at a matching radius r_m that is still in the nonrelativistic regime. However, we can see that close to the BH the system becomes spherically symmetric, as shown by the spherical contours of the Mach number.

For a perfect gas of index $\gamma = 5/3$, [138,139,143] found that the shock is attached to the BH (in their case the point mass as they consider Newtonian gravity) for moderate Mach numbers. In our case, we can clearly see that the bow shock is detached from the BH horizon and located at a radius of the order of r_{sg} for $v_0 \sim c_{s0}$. This is because of the

stiffer equation of state, $\gamma = 2$, which also significantly decreases the radial accretion rate (29) as compared with the usual Bondi result, as explained in Sec. II E. This property allows in turns the flow to become radial closer to the BH and confirms the analysis presented in Sec. V for moderate Mach numbers, with the accretion rate (86). The pattern of the flow is clearly seen by the velocity field shown in the lower-right panel, with a radial infall close to the BH and a stagnation point behind the BH along the z axis. At large distance the flow remains close to the uniform velocity \vec{v}_0 .

In the upper-left panel, the black straight solid line starting from the origin shows the Mach angle $\theta_c = \arcsin(c_{s0}/v_0)$ of Eq. (45). We can see that this agrees with the slope of the shock front at large distance. The blue solid line shows the sonic line where the Mach number crosses unity $\mathcal{M} = 1$. Its left part, which follows the shock, actually corresponds to the shock discontinuity where \mathcal{M} drops from $\mathcal{M}_{\text{upstream}} > 1$ to $\mathcal{M}_{\text{downstream}} < 1$. Therefore, although this line appears in the contour plot computed by VisIt, the Mach number is not unity on this line but crosses unity in a discontinuous manner. The right part, which runs from the shock to the z axis in the downstream region, is a true sonic line, where $\mathcal{M} = 1$. Indeed, whereas the shock efficiently slows down the incoming flow not too far from the BH, at large distance in the transverse plane the shock is weak and the velocity remains close to \vec{v}_0 . Thus, close to the z axis the flow becomes subsonic after the shock, while it remains supersonic at large distance. Moreover, far

downstream behind the BH the flow converges to the bulk velocity \vec{v}_0 and becomes again supersonic. Therefore, there is a finite-size region, behind the shock and enclosing the BH, where the flow is subsonic. This is marked by the sonic line shown by the blue solid line in the upper-left panel. It is within this subsonic region that the flow slows down and becomes approximately radial closer to the BH. Below the matching radius r_m and somewhat above the BH horizon, not shown in the plots, the flow becomes supersonic again and relativistic. Thus, there are actually two sonic lines.

As explained in Sec. V, at higher velocity we expect a strong asymmetry down to the horizon, with a shock that is no longer detached and a fully supersonic flow on the front side of the BH. However, this high-Mach regime is beyond the reach of our numerical code. We leave a detailed study of the accretion flow near the BH at these high Mach numbers to a future work. This has no impact on the result (83), which follows from the large-distance expansion, but it would be interesting to check the details of the transition (86)–(87). This regime is discussed in more detail in Appendix C, adapting the standard Bondi-Hoyle-Lyttleton analysis [132,133,144] to our case.

IX. COMPARISON WITH OTHER SYSTEMS

A. Mass accretion

The Bondi and Hoyle-Lyttleton accretion rates for a perfect gas are often computed with the expression

$$\dot{M}_{\text{BHL}} = \frac{4\pi\rho_0\mathcal{G}^2M_{\text{BH}}^2}{(c_{s0}^2 + v_0^2)^{3/2}}, \quad (99)$$

which interpolates between the subsonic and supersonic regimes [125,132,133]. As explained in Sec. V, at low velocities we have a smaller accretion rate, because of the more efficient self-interactions, whereas at high velocities we recover the Hoyle-Littleton prediction,

$$\begin{aligned} v_0 \ll c_{s0}^{2/3} : \dot{M}_{\text{BH}} &\ll \dot{M}_{\text{BHL}}, \\ v_0 \gg c_{s0}^{2/3} : \dot{M}_{\text{BH}} &\simeq \dot{M}_{\text{BHL}}. \end{aligned} \quad (100)$$

B. Dynamical friction

For a collisionless system, when the BH moves at a speed that is much greater than the velocity dispersion of the cloud particles the classical dynamical friction obtained by Chandrasekhar [114] (and confirmed by numerical simulations [145,146]) reads as

$$\text{collisionless: } F_{\text{free}} \simeq \frac{4\pi\rho_0\mathcal{G}^2M_{\text{BH}}^2}{v_0^2} \ln\left(\frac{b_{\text{max}}}{b_{\text{min}}}\right), \quad (101)$$

where b_{max} and b_{min} are large-scale and small-scale cutoffs. One usually takes $b_{\text{max}} = R$ given by the size of the cloud and $b_{\text{min}} = 2\mathcal{G}M_{\text{BH}}/v_0^2$ the critical impact parameter,

associated with bound orbits if their angular velocity is assumed to vanish when they meet the z axis behind the BH [133]. More generally, b_{min} corresponds to orbits with a deflection angle of order unity.

For the perfect gas, one obtains in the supersonic regime [129,147] (also recovered numerically, e.g. [148–150])

$$\text{perfect gas: } F_{\text{gas}} = \frac{4\pi\rho_0\mathcal{G}^2M_{\text{BH}}^2\mathcal{I}}{v_0^2}, \quad (102)$$

where $\mathcal{I} = \ln(1 - 1/\mathcal{M}^2)/2 + \ln(b_{\text{max}}/b_{\text{min}})$. In the case of $\mathcal{M} \gg 1$, the first term of \mathcal{I} vanishes, and only the second term (corresponding to a Coulomb logarithm) remains. Thus, this result is the same as (101).

Finally, in the case of FDM, with scalar masses around 10^{-22} eV where we can neglect dark matter self-interactions and the de Broglie wavelength is large, the dynamical friction is found to be [44]

$$\text{FDM: } F_{\text{FDM}} = \frac{4\pi\rho_0\mathcal{G}^2M_{\text{BH}}^2C(\beta, kr)}{v_0^2}. \quad (103)$$

Here, $C(\beta, kr)$ is given in terms of confluent hypergeometric functions, $\beta = \mathcal{G}M_{\text{BH}}m/v_0$ and $k = mv_0$. For $\beta \ll 1$ and $kr \gg 1$ one obtains $C \sim \ln(kr)$, which gives again an expression of the form of (101).

Therefore, in the supersonic regime all these systems give a dynamical friction that is similar to the Chandrasekhar result (101), except that the Coulomb logarithm can vary. This prefactor is usually difficult to estimate, and the infrared and ultraviolet cutoffs are often the result of an educated guess rather than an explicit derivation. In our case, the ultraviolet cutoff (91) is explicitly obtained from the analytic result (83). This is because in the steady state momentum conservation allows us to relate the drag force to the flux of momentum at large distance. Then, we have seen that r_{UV} is indeed the radius where the incoming velocity of the dark matter is significantly perturbed. This plays the role of the critical impact parameter $b_{\text{min}} \sim \mathcal{G}M_{\text{BH}}/v_0^2$ of the collisionless case. However, r_{UV} depends on the physics of the system and on the behavior of the self-interactions, as shown by its dependence on c_{s0} in (91). The infrared cutoff is then taken as the size of the cloud, as in other systems, with the peculiar property that this is not an additional parameter because for scalar dark matter with a quartic self-interaction it is independent of the mass of the cloud; see Eq. (25).

The radius r_{UV} of Eq. (91) is greater than the collisionless critical impact parameter $b_{\text{min}} \sim \mathcal{G}M_{\text{BH}}/v_0^2$,

$$r_{\text{UV}} \sim b_{\text{min}} \sqrt{\frac{v_0}{c_{s0}}}. \quad (104)$$

This is because of the collective pressure effects, which significantly modify the velocity field on small scales as

compared with the collisionless case, as discussed in Sec. [VIB](#). This makes the Coulomb logarithm [\(90\)](#) smaller than for the collisionless case, [\(101\)](#).

Apart from the logarithmic term, the prefactor in Eq. [\(90\)](#) is smaller than that in Eq. [\(101\)](#) by a factor of $2/3$. This value is confirmed by the computation [\(97\)](#) of the gravitational force from the BH wake at large distance. It is due to the physics of the dark matter fluid, where the self-interactions play a key role, as shown by the factor c_{s0} in the velocity and density jumps [\(96\)](#). In particular, it is determined by the effective polytropic equation of state $\gamma = 2$ of an isentropic flow, with its specific junction conditions. Thus, for a fixed cloud size the dynamical friction associated with SFDM is smaller than for CDM by at least a factor of $2/3$.

X. CONCLUSION

We have completed the study, started in [\[116\]](#), of the motion of a BH in a scalar dark matter cloud. Here we focus on the supersonic regime. This requires a deeper analysis than for the subsonic regime due to the appearance of a shock, as is usual for supersonic dynamics. Moreover, we found that at large distance this shock front is surrounded by two boundary layers, which introduce terms that scale as powers of $r^{-1/3}$ instead of r^{-1} in the large-distance expansion of the velocity potential. We have performed these large-distance expansions up to order r^{-2} for the density and velocity fields.

We showed how the large-distance expansions of the density and velocity fields can be related to the BH accretion rate, which is set by the small-scale boundary conditions at the Schwarzschild radius. This determines the remaining integration constant of the large-distance expansion, which is then closed in terms of the incoming velocity v_0 and of the accretion rate \dot{M}_{BH} . However, the value of \dot{M}_{BH} must be obtained by other means.

The large-distance expansion also provides the expression of the drag force experienced by the BH, thanks to the conservation of momentum. We find that the final result takes a simple form, which can be split as the sum of an accretion drag force, due to the accretion of dark matter by the BH, and a dynamical friction that takes a form similar to the classical Chandrasekhar result. However, the amplitude is decreased by a factor of $2/3$, and the Coulomb logarithm is finite, as it does not require the introduction of small- and large-scale cutoffs. The large-scale radius is set by the size R_{sol} of the dark matter soliton, which is a function of the combination m^4/λ_4 of the scalar-field parameters. The small-scale radius r_{UV} is generated by the dynamics of the flow and corresponds to the radius where the velocity field is significantly modified, with respect to the incoming velocity \bar{v}_0 . This radius is always much greater than the BH horizon, for nonrelativistic incoming velocities v_0 or sound speed c_{s0} . Thus, the

self-interactions provide a significant damping of the dynamical friction.

For moderate Mach numbers, $v_0 < c_{s0}^{2/3}$, we find that the accretion rate is still given by the radial prediction, which is much smaller than the Bondi-Hoyle-Lyttleton prediction. This is because of the stiff effective equation of state, with an adiabatic index $\gamma = 2$, which regulates the infall onto the BH near the Schwarzschild radius. Then, the bow shock is detached from the BH and located upstream of the BH. Behind the shock there is a subsonic region that encloses the BH and a stagnation point downstream. In this region the flow becomes approximately radial close to the BH. Closer to the Schwarzschild radius the flow becomes supersonic again, as in the radial case. This is confirmed by a numerical simulation for $\mathcal{M}_0 = 1.2$.

For high Mach numbers, $v_0 > c_{s0}^{2/3}$, we recover the Hoyle-Lyttleton accretion rate, which is then smaller than the one obtained in the radial case. Then, as in the classical Hoyle-Lyttleton analysis, most of the accretion takes place in the accretion column behind the BH, and the flow remains strongly asymmetric down to the Schwarzschild radius. The shock is then attached to the rear of the BH and forms the boundary of this narrow accretion column.

The mass accretion and dynamical friction provide invaluable insights about the surrounding environment of binary BHs, particularly the properties of the dark matter surrounding them. The dynamical friction exerted by the dark matter overdensity formed in the wake of the BHs introduces modifications to the waveforms, leading to a phase shift. The accretion of matter onto the BHs affects gravitational wave emission in a similar manner, but at a different post-Newtonian order. To exploit fully these effects and utilize them as probes of dark matter environments, improving our knowledge on the different dark matter models and enhancing the sensitivity of gravitational wave detectors is crucial. Advanced and upcoming detectors, such as Advanced LIGO, LISA and DECIGO, hold promising potential to enhance significantly our capacity to detect and analyze these effects. This analysis has been carried out for binary BHs in a companion paper [\[101\]](#). Future research in this direction holds great promise in shedding further light on the nature of dark matter and the astrophysical processes that shape the dynamics of binaries in galaxies.

ACKNOWLEDGMENTS

This work was granted access to the CCRT High-Performance Computing (HPC) facility under the Grant CCRT2023-valag awarded by the Fundamental Research Division (DRF) of CEA.

APPENDIX A: FREE CASE

In this Appendix, we consider the behavior of a cloud of fuzzy dark matter, that is, a scalar field without

self-interactions, moving at velocity \vec{v}_0 around a BH. This provides a reference point for comparison with the case of quartic self-interactions, i.e. the focus of this paper.

1. Schrödinger picture

Going back to the equation of motion in the form of the Schrödinger equation (13) for the complex scalar field ψ , the scattering of the incoming dark matter flux by the BH reads in the Newtonian regime

$$i\dot{\psi} = -\frac{\nabla^2\psi}{2m} + m\Phi_N\psi, \quad \Phi_N = -\frac{\mathcal{G}M_{\text{BH}}}{r}. \quad (\text{A1})$$

There is no self-interaction potential Φ_I , as we consider the free case in this appendix, and we neglect the self-gravity of the dark matter. This is a classic Coulomb scattering problem and we briefly recall the solution below [44,126]. We look for a steady-state solution of the form

$$\psi(\vec{x}, t) = e^{-iEt}\hat{\psi}(\vec{x}), \quad (\text{A2})$$

which is solution of the time-independent Schrödinger equation

$$\nabla^2\hat{\psi} + \left(2mE + 2m^2\frac{\mathcal{G}M}{r}\right)\hat{\psi} = 0. \quad (\text{A3})$$

The background case, without the BH, where the dark matter moves with the uniform velocity $\vec{v}_0 = v_0\vec{e}_z$, is given by

$$\tilde{\psi} = \sqrt{\frac{\bar{\rho}}{m}}e^{ikz}, \quad k = \sqrt{2mE} = mv_0. \quad (\text{A4})$$

Factoring out the background, one can check that the Schrödinger equation (A3) admits solutions of the form

$$\hat{\psi} = \sqrt{\frac{\bar{\rho}}{m}}e^{ikz}F(u), \quad u = r - z, \quad (\text{A5})$$

where $F(u)$ is solution of the differential equation

$$uF'' + (1 - iku)F' + \beta kF = 0, \quad \beta = \frac{\mathcal{G}M_{\text{BH}}m^2}{k}. \quad (\text{A6})$$

One can recognize the differential equation satisfied by the confluent hypergeometric equation $\Phi(\alpha, \gamma; z)$, and we obtain

$$\psi = \sqrt{\frac{\bar{\rho}}{m}}e^{-iEt+ikz}\Phi(i\beta, 1; ik(r-z)), \quad (\text{A7})$$

in agreement with [44]. At large distance, this gives the asymptotic form [126]

$$\psi \sim \sqrt{\frac{\bar{\rho}}{m}}e^{-iEt+ikz - i\frac{\mathcal{G}M_{\text{BH}}m^2}{k}\ln[k(r-z)]}. \quad (\text{A8})$$

The well-known logarithmic divergence of the correction to the background term is due to the long-range character of the Newton and Coulomb $1/r$ potentials.

2. Hydrodynamical picture

We now describe how this result can be recovered within the hydrodynamical picture used in this paper, in the large-scalar mass limit. Thus, we start from the Hamilton-Jacobi equation (17), where we take $\Phi_I = 0$ and Φ_N is given by Eq. (A1). At zeroth-order over the BH gravity, we recover the background solution (A4),

$$\tilde{\psi} = \sqrt{\frac{\bar{\rho}}{m}}e^{i\bar{s}}, \quad \bar{s} = -Et + kz, \quad k = \sqrt{2mE} = mv_0. \quad (\text{A9})$$

We factor out the background by introducing \hat{s} with

$$s = -Et + kz + \hat{s}(\vec{x}), \quad (\text{A10})$$

and we obtain at lowest order

$$\frac{\partial\hat{s}}{\partial z} = \frac{\mathcal{G}M_{\text{BH}}m^2}{kr}. \quad (\text{A11})$$

Looking again for a solution of the form $\hat{s}(u)$ with $u = r - z$, we obtain

$$\hat{s} = -\frac{\mathcal{G}M_{\text{BH}}m^2}{k}\ln[k(r-z)], \quad (\text{A12})$$

and hence

$$\psi = \sqrt{\frac{\bar{\rho}}{m}}e^{-iEt+ikz - i\frac{\mathcal{G}M_{\text{BH}}m^2}{k}\ln[k(r-z)]}. \quad (\text{A13})$$

We recover the asymptotic result (A8), with the logarithmic first-order correction that is characteristic of the $1/r$ Newtonian potential. This is only the leading-order result, upstream of the BH, and higher-order terms are generated by the nonlinearity of the continuity and Euler equations (16)–(17). We do not investigate this hydrodynamical approach further, as we focus on the case with nonzero self-interactions in this paper, and the free case is more conveniently described by the linear Schrödinger equation with the solution (A7).

We note however that in the large-mass limit the Hamilton-Jacobi equation provides a convenient tool to include general relativistic effects on the streamlines, as in Eq. (10), as it can be solved for the exact Schwarzschild metric functions f and h , without the need to use the Newtonian gravity approximation (6). This is because we

can explicitly solve the geodesic equations in the spherically symmetric Schwarzschild metric.

APPENDIX B: WIDTH OF THE BOUNDARY LAYER

In this Appendix, we describe how we can obtain the $\hat{r}^{2/3}$ scaling of the downstream boundary layer. At first order in the large-distance expansion, we have obtained in Sec. III C 1 the downstream bulk flow, given by Eq. (58). The velocity potential has a square-root singularity at the shock location u_c , as seen in Eq. (62). This leads to the divergent angular velocity (60) at u_c . Close to u_c , this first-order velocity perturbation $v_{\theta 1}$ becomes greater than the zeroth-order velocity v_0 . This signals the breakdown of this perturbative expansion. Therefore, nonlinear terms that have been neglected in this expansion must become important and regularize the angular velocity. Indeed, at sufficiently large distance we expect the shock to become increasingly weak and the velocity to converge to \vec{v}_0 (i.e., there is no divergence in the exact solution). Thanks to the factor $1/\hat{r}$ in Eq. (60) for $v_{\theta 1}$, the breakdown of the perturbative treatment appears at values u that are increasingly close to u_c at large distance. Therefore, the nonlinear correction to the divergent expression (60) occurs in an increasingly small region in u . This corresponds to a boundary-layer phenomenon, where nonlinear effects are restricted to a small region and permit the matching of a bulk solution with an adverse boundary condition. In our case, $1/\hat{r}$ plays the role of the small parameter ϵ of standard one-dimensional boundary-layer theory. The scaling of the boundary-layer width is often a power law of ϵ (here $1/\hat{r}$), but the exponent depends on the form of the nonlinear terms.

At lowest order, the shock front is located at u_c and the boundary-layer physics happens in the transverse direction, parallel to the angular velocity. Then, as in (58), we write for the phase

$$\hat{\beta} = v_0 \hat{r} u - \frac{\ln \hat{r}}{2v_0} + f_r(u), \quad (\text{B1})$$

but we do not assume that $f_r(u)$ is of order \hat{r}^0 in \hat{r} , which is why we added the subscript r . Instead, the dependence on \hat{r} is one of the boundary-layer scalings that we are looking for. As explained above, at lowest order the boundary-layer physics happens along the angular direction \vec{e}_θ ; the radial velocity remains finite, and it is only the angular velocity that diverges in (60). Therefore, derivatives will be dominated by angular derivatives. Besides, as the equation of motion (34) only involves $\widehat{\nabla} \hat{\beta}$, f_r only appears through its derivative, which we denote $g(u)$,

$$g(u) = f'_r(u). \quad (\text{B2})$$

We also define the transverse coordinate x as

$$u = u_c + x, \quad (\text{B3})$$

and we focus on the boundary layer with $x \ll 1$. To recover the flow \vec{v}_0 at large distance, the last term in Eq. (B1) must be subdominant with respect to the first term. This implies $g \ll \hat{r}$, that is, g grows more slowly than \hat{r} at large radii. On the other hand, the breakdown of the naive large-distance expansion of Sec. III C 1 means that we have $g \gg 1$. In the boundary layer, we have strong gradients as the fields evolve on the scale set by the boundary-layer width Δu , instead of the radius \hat{r} ; $g' \sim g/(\Delta u) \gg g/\hat{r}$. Thus, we have

$$x \ll 1, \quad 1 \ll g \ll \hat{r}, \quad g' \gg g/\hat{r}. \quad (\text{B4})$$

Then, we substitute the ansatz (B1) into the equation of motion (34), and we use the hierarchies (B4) to collect the dominant terms. This yields

$$xg' + \frac{1}{2}g - agg' = 0 \quad \text{with} \quad a = \frac{3c_z^2}{2v_0\sqrt{1+c_z^2}\hat{r}}. \quad (\text{B5})$$

We need to keep these three terms, as we do not know *a priori* the hierarchy between x , g and g' . Other terms in the equation of motion are suppressed with respect to one of these three terms by powers of x or g/\hat{r} .

In the large-distance expansion described in Sec. III C 1, we set $a = 0$ because of its $1/\hat{r}$ factor. This gives $xg' + g/2 = 0$, with the solution $g \propto 1/\sqrt{x}$. We recover the inverse square-root divergence of $v_{\theta 1}$ in Eq. (60) and of f'_0 from Eq. (62). Clearly, in this approximation, when $x \rightarrow 0^+$ the term agg' becomes greater than $g/2$, in spite of the smallness of a , and can no longer be neglected. This nonlinear term will then regularize the behavior at $x \rightarrow 0^+$. It is possible to obtain the exact analytical solution of the nonlinear differential equation (B5) in the implicit form

$$0 < x < \infty, \quad -\frac{b}{2a} < g < 0, \quad x = \frac{2a}{3}g + \frac{b^3}{12a^2}g^{-2}, \quad (\text{B6})$$

where b is an integration constant. From this expression we can derive the asymptotic expansions

$$\begin{aligned} x \rightarrow 0^+ : g &= -\frac{b}{2a} + \frac{x}{2a} + \dots, \\ x \rightarrow \infty : g &= -\frac{b^{3/2}}{2\sqrt{3}a\sqrt{x}} + \dots \end{aligned} \quad (\text{B7})$$

Thus, we can see that $g(x)$ is now regular at $x \rightarrow 0^+$. The divergence of the angular velocity has been regularized, and it remains finite up to the shock front. On the other hand, the asymptotic matching of the large- x behavior (B7) with the $u \rightarrow u_c^+$ behavior of the bulk flow (62) determines the integration constant b ,

$$b = \frac{3c_z^{2/3}(1+c_z^2)^{1/6}}{2^{1/3}v_0^{4/3}\hat{r}^{2/3}}. \quad (\text{B8})$$

The asymptotic scalings (B7), or the implicit solution (B6), show that the width of the boundary layer and the characteristic amplitude of g are

$$\Delta u = \Delta x \sim b \propto \hat{r}^{-2/3}, \quad g \sim \frac{b}{a} \propto \hat{r}^{1/3}. \quad (\text{B9})$$

These two scalings justify the $\hat{r}^{2/3}$ in the definition of the boundary-layer coordinate (67) and the $\hat{r}^{-1/3}$ that multiplies the F_1 term in Eq. (69) (so that it contributes at the order $\hat{r}^{1/3}$ in $\partial\hat{\beta}/\partial u$). Equation (B5) corresponds to Eq. (71), with different notations and the neglect of the shock curvature θ_1 .

The analysis above closely follows standard one-dimensional boundary-layer theory, and $1/\hat{r}$ plays the role of a small external parameter. As we go to higher orders, we need a more systematic approach that can handle our 2D problem, as radial derivatives and the curvature of the shock front start to contribute. This is done through the expansions (66)–(69). Because of the powers $\hat{r}^{1/3}$ that appear in (B9), we need a general expansion in powers of $\hat{r}^{-1/3}$. In addition, we must pay attention to the fact that logarithmic terms may appear. In Eqs. (66) and (69) we directly wrote those that are nonzero, after the computation is performed. The results obtained in Sec. III D 2 also show that the shock curvature θ_1 actually already contributes at the lowest order F_1 . However, this does not change the scalings (B9). Instead, this determines the scaling $\hat{r}^{-2/3}$ for the first curvature term in the expansion (66). We write a similar expansion (68) for the upstream boundary layer but as explained in the main text it starts at order $\hat{r}^{-2/3}$ instead of $\hat{r}^{-1/3}$ because the singularity of the upstream bulk flow at the shock is weaker.

APPENDIX C: ACCRETION COLUMN

1. Hoyle-Lyttleton accretion rate

We discuss in this Appendix the accretion on the BH in the high Mach number regime (87), where it proceeds through an accretion column on the rear side of the BH, as in the classical Hoyle-Lyttleton analysis. We use dimensional coordinates and closely follow the presentation of [133], adapted to our case. In the hypersonic regime, upstream of the shock front pressure effects are negligible and the dynamics follows the Keplerian orbits of the collisionless case. This gives for the streamline of impact parameter b the hyperbolic orbit

$$r = \frac{b^2 v_0^2}{\mathcal{G}M_{\text{BH}}(1 + \cos\theta) + b v_0^2 \sin\theta}, \quad (\text{C1})$$

with the radial and angular velocities

$$v_r = \pm \sqrt{v_0^2 + \frac{2\mathcal{G}M_{\text{BH}}}{r} - \frac{b^2 v_0^2}{r^2}}, \quad v_\theta = -\frac{b v_0}{r}, \quad (\text{C2})$$

and the density

$$\rho = \frac{\rho_0 b^2}{r \sin\theta(2b - r \sin\theta)}. \quad (\text{C3})$$

At high v_0 the accretion column is a roughly conical cylinder around the downstream z axis behind the shock front, with a narrow angle $\theta_s \ll 1$ that converges at large distances to the Mach angle θ_c of Eq. (45). From Eq. (C1), the orbit of impact parameter b crosses the downstream z axis $\theta = 0$ at the radius

$$r_1 = \frac{b^2 v_0^2}{2\mathcal{G}M_{\text{BH}}}, \quad (\text{C4})$$

with the velocities

$$v_{r_1} = v_0, \quad v_{\theta_1} = -\frac{2\mathcal{G}M_{\text{BH}}}{b v_0}. \quad (\text{C5})$$

This gives the boundary conditions upstream of the shock front, where we take $\theta_s \simeq 0$, while the density reads as

$$\rho_1 = \frac{\rho_0 \mathcal{G}M_{\text{BH}}}{\sin\theta_s b v_0^2}. \quad (\text{C6})$$

The junction conditions across the shock are the continuity of the tangential velocity and of the transverse momentum. Taking again $\theta_s \simeq 0$ this gives just behind the shock

$$v_{r_2} = v_0, \quad v_{\theta_2} = -\frac{c_{s0}^2}{\sin\theta_s v_0}, \quad \rho_2 = \frac{\rho_a \mathcal{G}M_{\text{BH}}}{r} = \frac{\rho_0 2\mathcal{G}^2 M_{\text{BH}}^2}{b^2 v_0^2 c_{s0}^2}, \quad (\text{C7})$$

where we used the Bernoulli equation

$$\frac{v^2}{2} + \frac{\rho}{\rho_a} - \frac{\mathcal{G}M_{\text{BH}}}{r} = \frac{v_0^2}{2} + \frac{\rho_0}{\rho_a}. \quad (\text{C8})$$

Indeed, in the subsonic regime just behind the BH we have $v^2 \ll c_s^2 = \rho/\rho_a$, which implies $\rho \simeq \rho_a \mathcal{G}M_{\text{BH}}/r$ for $r \lesssim \mathcal{G}M_{\text{BH}}/v_0^2$. For $\theta_s \sim \theta_c$ defined in Eq. (45) we obtain

$$\rho_1 \sim \frac{\rho_0 \mathcal{G}M_{\text{BH}}}{b v_0 c_{s0}}, \quad v_{\theta_2} \sim -c_{s0}. \quad (\text{C9})$$

If we neglect v_{θ_2} and assume that the dark matter will be accreted if it is bound to the BH, $v_0^2/2 - \mathcal{G}M_{\text{BH}}/r < 0$, we obtain the Hoyle-Lyttleton radius and impact parameter [133]

$$r_{\text{HL}} = \frac{2\mathcal{G}M_{\text{BH}}}{v_0^2}, \quad b_{\text{HL}} = \frac{2\mathcal{G}M_{\text{BH}}}{v_0^2}, \quad (\text{C10})$$

which gives the Hoyle-Lyttleton accretion rate $\dot{M}_{\text{HL}} = \rho_0 v_0 \pi b_{\text{HL}}^2$ of Eq. (85).

2. Approximate lower bound on the accretion rate

A more detailed analysis of the accretion column suggests that the accretion rate can be somewhat smaller [133]. From Eq. (C4), the mass flux that enters the accretion column through the shock between radii r and $r + dr$ is

$$F dr = \rho_0 v_0 2\pi b db = 2\pi \frac{\mathcal{G}M_{\text{BH}}\rho_0}{v_0} dr. \quad (\text{C11})$$

Denoting μdr the mass in the accretion column between radii r and $r + dr$ and v the mean longitudinal velocity in the column, the conservation of matter gives

$$\frac{d}{dr}(\mu v) = F, \quad (\text{C12})$$

whereas the conservation of longitudinal momentum gives

$$\frac{d}{dr}(\mu v^2) = -\frac{\mathcal{G}M_{\text{BH}}\mu}{r^2} + \frac{d}{dr}(\pi r_{\perp}^2 P) + F v_0, \quad (\text{C13})$$

where the first term on the right-hand side is the gravitational attraction from the BH, the second term is the pressure force, and the third term is the momentum inflow as $v_2 = v_0$ on the shock. As the pressure reads $P = \rho^2/(2\rho_a)$, we find that in contrast with the Bondi-Hoyle analysis [133,144] the pressure is *a priori* of the same order as the gravitational energy, $r_{\perp}^2 P \sim \mathcal{G}M_{\text{BH}}\mu/r \sim \rho_0 \mathcal{G}^2 M_{\text{BH}}^2 / v_0^2$. However, for a conical shock with a constant angle θ_s we have $r_{\perp} \propto r$ while $P \propto \rho^2 \propto r^{-2}$, so that the derivative of the pressure term vanishes. Therefore, the pressure term is suppressed as compared with the gravitational term, and the analysis can proceed as in [133,144]. The mass conservation equation (C12) can be integrated as

$$\mu v = F(r - r_0), \quad (\text{C14})$$

where r_0 is the location of the stagnation point behind the BH. The momentum conservation equation (C13) can be written as

$$v \frac{dv}{dr} = -\frac{\mathcal{G}M_{\text{BH}}}{r^2} + \frac{v(v_0 - v)}{r - r_0}. \quad (\text{C15})$$

Then, requiring the velocity to be a monotonic function, from -1 close to the BH to v_0 at infinity, implies [133]

$$r_0 > \frac{\mathcal{G}M_{\text{BH}}}{v_0^2}. \quad (\text{C16})$$

Then the accretion rate is bounded from below by

$$\dot{M}_{\text{BH}} = \int_0^{r_0} dr F = F r_0 > \frac{2\pi\rho_0 \mathcal{G}^2 M_{\text{BH}}^2}{v_0^3}, \quad (\text{C17})$$

which is twice as small as the Hoyle-Lyttleton accretion rate (85).

3. Velocity threshold for the accretion-column regime

At radii of the order of the Schwarzschild radius inside the accretion column we have $\rho \sim \rho_a$ and $v \sim -1$. As seen from the Bernoulli equation (C8), these are the highest possible density and velocity (at the limit of the Newtonian regime). They are also reached in the radial accretion case. The solid angle Ω of the accretion column at a radius of the order of r_s is then related to the accretion rate by

$$\Omega r_s^2 \rho_a \sim \dot{M}_{\text{BH}} \sim \rho_0 \mathcal{G}^2 M_{\text{BH}}^2 / v_0^3, \quad (\text{C18})$$

which gives

$$\Omega \sim \frac{c_{s0}^2}{v_0^3}, \quad \text{whence } \Omega \gtrsim 1 \quad \text{when } v_0 \lesssim c_{s0}^{2/3}. \quad (\text{C19})$$

Thus we recover the two regimes (86)–(87). For $v_0 > c_{s0}^{2/3}$ the accretion column is narrow behind the BH and the accretion rate is of the order of the Hoyle-Lyttleton prediction. For $v_0 < c_{s0}^{2/3}$ the accretion column is large and actually engulfs all sides of the BH. There is now a bow shock upstream of the BH, as seen in the numerical computation displayed in Fig. 1, and the accretion rate is much smaller than the Bondi-Hoyle-Lyttleton prediction, because of the strong impact of the self-interactions in this subsonic region.

From Eqs. (C1)–(C3) we can see that in the high Mach regime, $v_0 > c_{s0}^{2/3}$, the density and the velocity at $r \sim r_s$ on the upstream face of the BH, at $\theta = \pi$, are

$$v_r \sim 1, \quad \rho \sim \rho_a \frac{c_{s0}^2}{v_0} < \rho_a c_{s0}^{4/3} \ll \rho_a. \quad (\text{C20})$$

This confirms that this regime is very asymmetric, with a low infall rate on the upstream face of the BH, low densities and negligible self-interactions. This allows the matter to fall directly into the BH while remaining in the supersonic regime and without crossing a shock, over most of the BH surface. However, most of the accretion rate comes from the narrow accretion column at the back of the BH, which is associated with an attached shock and a finite-size subsonic region.

- [1] N. Aghanim *et al.* (Planck Collaboration), *Astron. Astrophys.* **641**, A6 (2020); **652**, C4(E) (2021).
- [2] C. Doux *et al.* (DES Collaboration), *Mon. Not. R. Astron. Soc.* **515**, 1942 (2022).
- [3] J. L. Feng, H. Tu, and H.-B. Yu, *J. Cosmol. Astropart. Phys.* **10** (2008) 043.
- [4] D. Hooper, in *The Dawn of the LHC Era* (World Scientific, Singapore, 2010).
- [5] D. J. Schwarz, *Ann. Phys. (Amsterdam)* **12**, 220 (2003).
- [6] S. Chang, R. Edezhath, J. Hutchinson, and M. Luty, *Phys. Rev. D* **89**, 015011 (2014).
- [7] M. A. G. Garcia, K. Kaneta, Y. Mambrini, K. A. Olive, and S. Verner, *J. Cosmol. Astropart. Phys.* **03** (2022) 016.
- [8] J. L. Feng, *SciPost Phys. Lect. Notes* **71**, 1 (2023).
- [9] J. Liu, X. Chen, and X. Ji, *Nat. Phys.* **13**, 212 (2017).
- [10] J. Billard *et al.*, *Rep. Prog. Phys.* **85**, 056201 (2022).
- [11] L. Roszkowski, E. M. Sessolo, and S. Trojanowski, *Rep. Prog. Phys.* **81**, 066201 (2018).
- [12] G. Arcadi, M. Dutra, P. Ghosh, M. Lindner, Y. Mambrini, M. Pierre, S. Profumo, and F. S. Queiroz, *Eur. Phys. J. C* **78**, 203 (2018).
- [13] L. Hui, *Phys. Rev. Lett.* **86**, 3467 (2001).
- [14] W. J. G. de Blok, *Adv. Astron.* **2010**, 789293 (2010).
- [15] S.-H. Oh, C. Brook, F. Governato, E. Brinks, L. Mayer, W. J. G. de Blok, A. Brooks, and F. Walter, *Astron. J.* **142**, 24 (2011).
- [16] R. Teyssier, A. Pontzen, Y. Dubois, and J. Read, *Mon. Not. R. Astron. Soc.* **429**, 3068 (2013).
- [17] J. I. Read, O. Agertz, and M. L. M. Collins, *Mon. Not. R. Astron. Soc.* **459**, 2573 (2016).
- [18] A. A. Klypin, A. V. Kravtsov, O. Valenzuela, and F. Prada, *Astrophys. J.* **522**, 82 (1999).
- [19] L. E. Strigari, J. S. Bullock, M. Kaplinghat, J. Diemand, M. Kuhlen, and P. Madau, *Astrophys. J.* **669**, 676 (2007).
- [20] Q. Guo, S. White, M. Boylan-Kolchin, G. De Lucia, G. Kauffmann, G. Lemson, C. Li, V. Springel, and S. Weinmann, *Mon. Not. R. Astron. Soc.* **413**, 101 (2011).
- [21] J. Penarrubia, A. Pontzen, M. G. Walker, and S. E. Kroupa, *Astrophys. J. Lett.* **759**, L42 (2012).
- [22] M. Boylan-Kolchin, J. S. Bullock, and M. Kaplinghat, *Mon. Not. R. Astron. Soc.* **415**, L40 (2011).
- [23] S. Garrison-Kimmel, M. Boylan-Kolchin, J. S. Bullock, and E. N. Kirby, *Mon. Not. R. Astron. Soc.* **444**, 222 (2014).
- [24] M. Kaplinghat, M. Valli, and H.-B. Yu, *Mon. Not. R. Astron. Soc.* **490**, 231 (2019).
- [25] M. S. Pawlowski, B. Famaey, D. Merritt, and P. Kroupa, *Astrophys. J.* **815**, 19 (2015).
- [26] P. Ivanov, P. Naselsky, and I. Novikov, *Phys. Rev. D* **50**, 7173 (1994).
- [27] S. Clesse and J. García-Bellido, *Phys. Rev. D* **92**, 023524 (2015).
- [28] B. Carr, F. Kuhnel, and M. Sandstad, *Phys. Rev. D* **94**, 083504 (2016).
- [29] B. Carr and F. Kuhnel, *Annu. Rev. Nucl. Part. Sci.* **70**, 355 (2020).
- [30] A. M. Green and B. J. Kavanagh, *J. Phys. G* **48**, 043001 (2021).
- [31] L. D. Duffy and K. van Bibber, *New J. Phys.* **11**, 105008 (2009).
- [32] D. J. E. Marsh, *Phys. Rep.* **643**, 1 (2016).
- [33] J. E. Kim and G. Carosi, *Rev. Mod. Phys.* **82**, 557 (2010); **91**, 049902(E) (2019).
- [34] P. W. Graham, I. G. Irastorza, S. K. Lamoreaux, A. Lindner, and K. A. van Bibber, *Annu. Rev. Nucl. Part. Sci.* **65**, 485 (2015).
- [35] I. G. Irastorza and J. Redondo, *Prog. Part. Nucl. Phys.* **102**, 89 (2018).
- [36] L. Di Luzio, M. Giannotti, E. Nardi, and L. Visinelli, *Phys. Rep.* **870**, 1 (2020).
- [37] S. Dodelson and L. M. Widrow, *Phys. Rev. Lett.* **72**, 17 (1994).
- [38] X.-D. Shi and G. M. Fuller, *Phys. Rev. Lett.* **82**, 2832 (1999).
- [39] A. Boyarsky, O. Ruchayskiy, and M. Shaposhnikov, *Annu. Rev. Nucl. Part. Sci.* **59**, 191 (2009).
- [40] A. Kusenko, *Phys. Rep.* **481**, 1 (2009).
- [41] J. L. Feng, *Annu. Rev. Astron. Astrophys.* **48**, 495 (2010).
- [42] K. N. Abazajian *et al.*, arXiv:1204.5379.
- [43] W. Hu, R. Barkana, and A. Gruzinov, *Phys. Rev. Lett.* **85**, 1158 (2000).
- [44] L. Hui, J. P. Ostriker, S. Tremaine, and E. Witten, *Phys. Rev. D* **95**, 043541 (2017).
- [45] S. Knapen, T. Lin, and K. M. Zurek, *Phys. Rev. D* **96**, 115021 (2017).
- [46] E. G. M. Ferreira, *Astron. Astrophys. Rev.* **29**, 7 (2021).
- [47] L. Hui, *Annu. Rev. Astron. Astrophys.* **59**, 247 (2021).
- [48] J. Goodman, *New Astron.* **5**, 103 (2000).
- [49] H.-Y. Schive, T. Chiueh, and T. Broadhurst, *Nat. Phys.* **10**, 496 (2014).
- [50] H.-Y. Schive, M.-H. Liao, T.-P. Woo, S.-K. Wong, T. Chiueh, T. Broadhurst, and W. Y. P. Hwang, *Phys. Rev. Lett.* **113**, 261302 (2014).
- [51] A. Arbey, J. Lesgourgues, and P. Salati, *Phys. Rev. D* **64**, 123528 (2001).
- [52] P.-H. Chavanis, *Phys. Rev. D* **84**, 043531 (2011).
- [53] P. H. Chavanis and L. Delfini, *Phys. Rev. D* **84**, 043532 (2011).
- [54] D. J. E. Marsh and A.-R. Pop, *Mon. Not. R. Astron. Soc.* **451**, 2479 (2015).
- [55] E. Calabrese and D. N. Spergel, *Mon. Not. R. Astron. Soc.* **460**, 4397 (2016).
- [56] S.-R. Chen, H.-Y. Schive, and T. Chiueh, *Mon. Not. R. Astron. Soc.* **468**, 1338 (2017).
- [57] B. Schwabe, J. C. Niemeyer, and J. F. Engels, *Phys. Rev. D* **94**, 043513 (2016).
- [58] J. Veltmaat and J. C. Niemeyer, *Phys. Rev. D* **94**, 123523 (2016).
- [59] A. X. González-Morales, D. J. E. Marsh, J. Peñarrubia, and L. A. Ureña López, *Mon. Not. R. Astron. Soc.* **472**, 1346 (2017).
- [60] V. H. Robles and T. Matos, *Mon. Not. R. Astron. Soc.* **422**, 282 (2012).
- [61] T. Bernal, L. M. Fernández-Hernández, T. Matos, and M. A. Rodríguez-Meza, *Mon. Not. R. Astron. Soc.* **475**, 1447 (2018).
- [62] P. Mocz, M. Vogelsberger, V. H. Robles, J. Zavala, M. Boylan-Kolchin, A. Fialkov, and L. Hernquist, *Mon. Not. R. Astron. Soc.* **471**, 4559 (2017).

- [63] K. Mukaida, M. Takimoto, and M. Yamada, *J. High Energy Phys.* **03** (2017) 122.
- [64] J. Vicens, J. Salvado, and J. Miralda-Escudé, arXiv:1802.10513.
- [65] N. Bar, D. Blas, K. Blum, and S. Sibiryakov, *Phys. Rev. D* **98**, 083027 (2018).
- [66] J. Eby, K. Mukaida, M. Takimoto, L. C. R. Wijewardhana, and M. Yamada, *Phys. Rev. D* **99**, 123503 (2019).
- [67] B. Bar-Or, J.-B. Fouvry, and S. Tremaine, *Astrophys. J.* **871**, 28 (2019).
- [68] D. J. E. Marsh and J. C. Niemeyer, *Phys. Rev. Lett.* **123**, 051103 (2019).
- [69] P.-H. Chavanis, *Phys. Rev. D* **100**, 083022 (2019).
- [70] R. Emami, T. Broadhurst, G. Smoot, T. Chiueh, and H. N. Luu, *Phys. Rev. D* **101**, 063006 (2020).
- [71] D. G. Levkov, A. G. Panin, and I. I. Tkachev, *Phys. Rev. Lett.* **121**, 151301 (2018).
- [72] T. Broadhurst, I. de Martino, H. N. Luu, G. F. Smoot, and S. H. H. Tye, *Phys. Rev. D* **101**, 083012 (2020).
- [73] K. Hayashi and I. Obata, *Mon. Not. R. Astron. Soc.* **491**, 615 (2020).
- [74] N. Bar, K. Blum, J. Eby, and R. Sato, *Phys. Rev. D* **99**, 103020 (2019).
- [75] R. G. García, P. Brax, and P. Valageas, arXiv:2304.10221.
- [76] M. C. Johnson and M. Kamionkowski, *Phys. Rev. D* **78**, 063010 (2008).
- [77] J.-c. Hwang and H. Noh, *Phys. Lett. B* **680**, 1 (2009).
- [78] C.-G. Park, J.-c. Hwang, and H. Noh, *Phys. Rev. D* **86**, 083535 (2012).
- [79] R. Hlozek, D. Grin, D. J. E. Marsh, and P. G. Ferreira, *Phys. Rev. D* **91**, 103512 (2015).
- [80] J. A. R. Cembranos, A. L. Maroto, and S. J. Núñez Jareño, *J. High Energy Phys.* **03** (2016) 013.
- [81] L. A. Ureña-López and A. X. Gonzalez-Morales, *J. Cosmol. Astropart. Phys.* **07** (2016) 048.
- [82] L. A. Ureña López, *Front. Astron. Space Sci.* **6**, 47 (2019).
- [83] V. Iršič, M. Viel, M. G. Haehnelt, J. S. Bolton, and G. D. Becker, *Phys. Rev. Lett.* **119**, 031302 (2017).
- [84] E. Armengaud, N. Palanque-Delabrouille, C. Yèche, D. J. E. Marsh, and J. Baur, *Mon. Not. R. Astron. Soc.* **471**, 4606 (2017).
- [85] J. Zhang, J.-L. Kuo, H. Liu, Y.-L. S. Tsai, K. Cheung, and M.-C. Chu, *Astrophys. J.* **863**, 73 (2018).
- [86] N. Bar, K. Blum, and C. Sun, *Phys. Rev. D* **105**, 083015 (2022).
- [87] M. C. Bento, O. Bertolami, R. Rosenfeld, and L. Teodoro, *Phys. Rev. D* **62**, 041302 (2000).
- [88] A. Riotto and I. Tkachev, *Phys. Lett. B* **484**, 177 (2000).
- [89] D. Fregolente and M. D. Tonasse, *Phys. Lett. B* **555**, 7 (2003).
- [90] B. Li, T. Rindler-Daller, and P. R. Shapiro, *Phys. Rev. D* **89**, 083536 (2014).
- [91] A. Suárez and P.-H. Chavanis, *Phys. Rev. D* **92**, 023510 (2015).
- [92] A. Suárez and P.-H. Chavanis, *Phys. Rev. D* **95**, 063515 (2017).
- [93] A. Suárez and P.-H. Chavanis, *Phys. Rev. D* **98**, 083529 (2018).
- [94] P. Brax, J. A. R. Cembranos, and P. Valageas, *Phys. Rev. D* **100**, 023526 (2019).
- [95] P. Brax, P. Valageas, and J. A. R. Cembranos, *Phys. Rev. D* **101**, 023521 (2020).
- [96] B. Dave and G. Goswami, *J. Cosmol. Astropart. Phys.* **07** (2023) 015.
- [97] L. H. Thomas, *Math. Proc. Cambridge Philos. Soc.* **23**, 542 (1927).
- [98] E. Fermi, *R. Accad. Naz. Lincei.* **6**, 602 (1927).
- [99] K. Eda, Y. Itoh, S. Kuroyanagi, and J. Silk, *Phys. Rev. Lett.* **110**, 221101 (2013).
- [100] B. J. Kavanagh, D. A. Nichols, G. Bertone, and D. Gaggero, *Phys. Rev. D* **102**, 083006 (2020).
- [101] A. Boudon, P. Brax, P. Valageas, and L. K. Wong, arXiv:2305.18540.
- [102] N. Bar, K. Blum, T. Lacroix, and P. Pani, *J. Cosmol. Astropart. Phys.* **07** (2019) 045.
- [103] S. Chakrabarti, B. Dave, K. Dutta, and G. Goswami, *J. Cosmol. Astropart. Phys.* **09** (2022) 074.
- [104] Y. Ravanal, G. Gómez, and N. Cruz, *Phys. Rev. D* **108**, 083004 (2023).
- [105] L. Berezhiani, B. Elder, and J. Khoury, *J. Cosmol. Astropart. Phys.* **10** (2019) 074.
- [106] L. Lancaster, C. Giovanetti, P. Mocz, Y. Kahn, M. Lisanti, and D. N. Spergel, *J. Cosmol. Astropart. Phys.* **01** (2020) 001.
- [107] S. T. H. Hartman, H. A. Winther, and D. F. Mota, *Astron. Astrophys.* **647**, A70 (2021).
- [108] L. Annulli, V. Cardoso, and R. Vicente, *Phys. Rev. D* **102**, 063022 (2020).
- [109] Y. Wang and R. Easther, *Phys. Rev. D* **105**, 063523 (2022).
- [110] D. Traykova, K. Clough, T. Helfer, E. Berti, P. G. Ferreira, and L. Hui, *Phys. Rev. D* **104**, 103014 (2021).
- [111] D. D. Chowdhury, F. C. van den Bosch, V. H. Robles, P. van Dokkum, H.-Y. Schive, T. Chiueh, and T. Broadhurst, *Astrophys. J.* **916**, 27 (2021).
- [112] R. Vicente and V. Cardoso, *Phys. Rev. D* **105**, 083008 (2022).
- [113] D. Traykova, R. Vicente, K. Clough, T. Helfer, E. Berti, P. G. Ferreira, and L. Hui, arXiv:2305.10492.
- [114] S. Chandrasekhar, *Astrophys. J.* **97**, 255 (1943).
- [115] N. Bar, D. Blas, K. Blum, and H. Kim, *Phys. Rev. D* **104**, 043021 (2021).
- [116] A. Boudon, P. Brax, and P. Valageas, *Phys. Rev. D* **106**, 043507 (2022).
- [117] C. F. B. Macedo, P. Pani, V. Cardoso, and L. C. B. Crispino, *Astrophys. J.* **774**, 48 (2013).
- [118] E. Barausse, V. Cardoso, and P. Pani, *Phys. Rev. D* **89**, 104059 (2014).
- [119] V. Cardoso and A. Maselli, *Astron. Astrophys.* **644**, A147 (2020).
- [120] G.-L. Li, Y. Tang, and Y.-L. Wu, *Sci. China Phys. Mech. Astron.* **65**, 100412 (2022).
- [121] I. S. Gradshteyn and I. M. Ryzhik, *Table of Integrals, Series, and Products*, 4th ed. (Academic Press, New York 1965).
- [122] P. Byrd and M. Friedman, *Handbook of Elliptic Integrals for Engineers and Scientists* (Springer, Berlin, Heidelberg, 1971).
- [123] I. Kovacic and M. Brennan, *The Duffing Equation: Non-linear Oscillators and their Behaviour* (Wiley, New York, 2011).

- [124] E. Madelung, *Z. Phys.* **40**, 322 (1927).
- [125] H. Bondi, *Mon. Not. R. Astron. Soc.* **112**, 195 (1952).
- [126] N. F. Mott and H. S. W. Massey, *The Theory of Atomic Collisions*, T. I. S. of Monographs on Physics, Vol. 35 (Clarendon Press Oxford, Oxford, 1965).
- [127] Tam and C. K. W., *Phys. Fluids* **9**, 493 (1966).
- [128] V. P. Dokuchaev, *Sov. Astron.* **8**, 23 (1964).
- [129] M. A. Ruderman and E. A. Spiegel, *Astrophys. J.* **165**, 1 (1971).
- [130] C. Hirsch, *Numerical Computation of Internal and External Flows* (Elsevier, New York, 2007).
- [131] S. Orszag and C. M. Bender, *Advanced Mathematical Methods for Scientists and Engineers* (McGraw-Hill, New York, 1978).
- [132] F. Hoyle and R. A. Lyttleton, *Proc. Cambridge Philos. Soc.* **35**, 405 (1939).
- [133] R. G. Edgar, *New Astron. Rev.* **48**, 843 (2004).
- [134] W. A. Mulder, Mulder, and W. A., *Astron. Astrophys.* **117**, 9 (1983).
- [135] R. Keppens, B. Popescu Braileanu, Y. Zhou, W. Ruan, C. Xia, Y. Guo, N. Claes, and F. Bacchini, *Astron. Astrophys.* **673**, A66 (2023).
- [136] R. Keppens, J. Teunissen, C. Xia, and O. Porth, *Comput. Math. Appl.* **81**, 316 (2021).
- [137] <https://amrvac.org/index.html>.
- [138] I. E. Mellah and F. Casse, *Mon. Not. R. Astron. Soc.* **454**, 2657 (2015).
- [139] C. Xia, J. Teunissen, I. E. Mellah, E. Chané, and R. Keppens, *Astrophys. J. Suppl. Ser.* **234**, 30 (2018).
- [140] E. F. Toro, M. Spruce, and W. Speares, *Shock Waves* **4**, 25 (1994).
- [141] H. Childs, E. Brugger, B. Whitlock, J. Meredith, S. Ahern, D. Pugmire, K. Biagas, M. Miller, C. Harrison, G. H. Weber *et al.*, in *High Performance Visualization—Enabling Extreme-Scale Scientific Insight* (Chapman and Hall/CRC, New York, 2012), pp. 357–372.
- [142] <https://visit-dav.github.io/visit-website/>.
- [143] T. Foglizzo and M. Ruffert, *Astron. Astrophys.* **320**, 342 (1997).
- [144] H. Bondi and F. Hoyle, *Mon. Not. R. Astron. Soc.* **104**, 273 (1944).
- [145] F. Antonini and D. Merritt, *Astrophys. J.* **745**, 83 (2011).
- [146] J. Binney and S. Tremaine, *Galactic Dynamics* (Princeton University Press, New Jersey, 1987), p. 747.
- [147] E. C. Ostriker, *Astrophys. J.* **513**, 252 (1999).
- [148] F. J. Sánchez-Salcedo and A. Brandenburg, *Astrophys. J.* **522**, L35 (1999).
- [149] C. G. Bernal and F. J. Sanchez-Salcedo, *Astrophys. J.* **775**, 72 (2013).
- [150] D. Thun, R. Kuiper, F. Schmidt, and W. Kley, *Astron. Astrophys.* **589**, A10 (2016).